REACTIVE ION ENHANCED MAGNETRON SPUTTERING OF NITRIDE THIN FILMS

By

Al-Ahsan Talukder

A DISSERTATION

Submitted to
Michigan State University
in partial fulfillment of the requirements
for the degree of

Electrical Engineering – Doctor of Philosophy

2022

ABSTRACT

REACTIVE ION ENHANCED MAGNETRON SPUTTERING OF NITRIDE THIN FILMS

By

Al-Ahsan Talukder

Magnetron sputtering is a popular vacuum plasma coating technique used for depositing metals, dielectrics, semiconductors, alloys, and compounds onto a wide range of substrates. In this work, we present two popular types of magnetron sputtering, i.e., pulsed DC and RF magnetron sputtering, for depositing piezoelectric aluminum nitride (AlN) thin films with high Young's modulus. The effects of important process parameters on the plasma I-V characteristics, deposition rate, and the properties of the deposited AlN films, are studied comprehensively. The effects of these process parameters on Young's modulus of the deposited films are also presented. Scanning electron microscope imaging revealed a c-axis oriented columnar growth of AlN. Performance of surface acoustic devices, utilizing the AlN films deposited by magnetron sputtering, are also presented, which confirms the differences in qualities and microstructures of the pulsed DC and RF sputtered films. The RF sputtered AlN films showed a denser microstructure with smaller grains and a smoother surface than the pulsed DC sputtered films. However, the deposition rate of RF sputtering is about half of the pulsed DC sputtering process.

We also present a novel ion source enhanced pulsed DC magnetron sputtering for depositing high-quality nitrogen-doped zinc telluride (ZnTe:N) thin films. This ion source enhanced magnetron sputtering provides an increased deposition rate, efficient N-doping, and improved electrical, structural, and optical properties than the traditional magnetron sputtering. Ion source enhanced deposition leads to ZnTe:N films with smaller lattice spacing and wider X-

ray diffraction peak, which indicates denser films with smaller crystallites embedded in an amorphous matrix.

ACKNOWLEDGEMENTS

First and foremost, I would like to express my heartiest gratitude to my PhD advisor, Dr. Qi Hua Fan for providing me with an opportunity to work as a graduate research assistant in his research group at Michigan State University. Since the beginning of my graduate study, he has provided me with endless supervision, guidance, and support. Dr. Fan has made a world of difference in many aspects of my academic, professional, and personal development.

I also offer my deepest gratitude to the PhD committee members for guiding my research in the proper direction. They provided me with essential and compelling suggestions to improve the writing of my dissertation. Their scholarly suggestions made my research so much richer, so I can be proud of my dissertation.

I am also grateful to Nina Baule, Maximilian Steinhorst, Robert Rechenberg, and Dr. Maheshwar Shrestha from Fraunhofer USA Center Midwest CMW, for their support and cooperation during this research work. This research work was supported by the Department of Electrical and Computer Engineering, Michigan State University, and Fraunhofer USA Center Midwest CMW.

Last but not the least, I would also like to thank my beloved wife and family members back in Bangladesh for their continuous love and support.

TABLE OF CONTENTS

LIST OF TABLES

LIST OF FIGURES

CHAPTER 1: INTRODUCTION

1.1. Background and Motivation

Reactive sputtering is widely used for making nitride and oxide films. The reactive process can occur (i) on the target surface, (ii) on the substrate surface, and (iii) in the gas phase during target atom transport. Most of the reactive processes occur on the substrate and target surface where the energy of formation can easily be dissipated without decomposing the newly formed compound. Reaction in the gaseous phase is insignificant since the energy of formation and kinetic energy of the atoms cannot be dissipated, causing a spontaneous decomposition of any compound as it is formed [1–3].

When the reactive gas is used in sufficient concentration, intensive reactions occur at the target surface (cathode); the resultant species are then transported to the substrate (grounded anode). The reactive process that occurs on the target surface causes the formation of a compound on the target surface, which is often termed “target poisoning”. When this compound is an insulator and a direct-current (DC) power supply is used, succeeding positive ion bombardments lead to charge accumulation on the target surface, which causes arcing that is detrimental to the film quality. Using a pulsed DC or radio frequency (RF) power supply, this target poisoning and charging effect can be overcome [1,2]

The reactive process that occurs on the substrate surface is critical to the microstructure and properties of the deposited film [1,2]. Atomic reactive species and ions have much stronger reactions with the deposited films. Therefore, creating a high flux of reactive species (atoms, excited molecules, and ions) is the primary consideration in the reactive sputtering deposition. DC and RF sputtering create different plasma potentials between the cathode (sputter target) and anode (substrate). Specifically, RF discharge creates a much larger potential drop between the bulk plasma and the substrate as compared with DC discharge [4]. Hence, we hypothesize that RF sputtering can deliver energetic ions to bombard the films, enhancing the reactions and modulating the film microstructures.

To evaluate the effects of the energetic ions in reactive sputtering, we first examine aluminum nitride (AlN) piezoelectric films produced by DC and RF sputtering. We selected AlN because the piezoelectric properties strongly depend on the packing density and micro-voids [5]. On the other hand, although RF sputtering provides the possibility of ion bombardment to the growing film, it could not easily and independently adjust the ion energy and flux. Therefore, we study ion source enhanced reactive sputtering, in which controlled ion energy and flux can be delivered to the growing film to achieve optimum ion-atom interactions.

Conventional ion sources have limitations, such as being incompatible with reactive gases and unstable when operating with a magnetron. Therefore, we developed and tested an alternative single beam ion/plasma source to enhance reactive magnetron sputtering [6]. We choose nitrogen-doped zinc telluride (ZnTe:N) for this study because it is challenging to effectively dope active N-atoms in the zinc telluride (ZnTe) compounds under common magnetron sputtering conditions. ZnTe:N is an important photovoltaic material in ZnTe thin-film solar cells. While high-quality ZnTe:N thin films have been demonstrated by RF sputtering at low deposition rates, we hypothesize that ion source enhanced DC sputtering can produce high-quality ZnTe:N films at high rates, which is particularly interesting for mass production.

In this research, we study AlN films formed by magnetron sputtering through systematic investigation of the pulsed DC and RF discharge parameters and thorough characterization of the surface, structural, and mechanical properties of the films. We demonstrate that pulsed DC sputtering offers a high deposition rate sacrificing the film quality and RF sputtering can produce high-quality films with smooth surfaces and high packing density, sacrificing the deposition rate. Finally, we deposit ZnTe:N thin films using ion source enhanced pulsed DC magnetron sputtering which offers a high deposition rate, and most importantly the ability to modulate the doping level, conductivity, and optical property of the film, by adjusting the ion source voltage.

1.2. Organization of This Dissertation

This dissertation is organized into five chapters, with this introduction being Chapter 1. The background and motivation of the research are laid out in Chapter 1. Chapter 2 discusses the basics of magnetron sputtering deposition and thin film characterization tools. The discussion on magnetron sputtering deposition includes, DC magnetron sputtering, pulsed DC magnetron sputtering, RF sputtering, and finally, the proposed ion source enhanced magnetron sputtering. Chapter 2 also presents some fundamental descriptions of thin-film characterization tools including, laser acoustic wave analysis (LAwave), scanning probe microscopy (SPM), and x-ray diffraction analysis (XRD).

Chapter 3 presents a comprehensive baseline study of pulsed DC reactive sputtering of AlN thin films. The study includes the effects of process pressure, process gas composition, pulse frequency, and pulse duty cycle, on the deposited film's properties. The deposition process is characterized using I-V characteristics and deposition rate analysis. The film's properties are characterized using surface roughness, x-ray diffraction scan, and Young's modulus analysis. This chapter also presents a scanning electron microscope (SEM) image of the cross-sectional of the optimized pulsed DC sputtered AlN film. This chapter also presents the reflection coefficient measurement result of surface acoustic (SAW) devices fabricated using the optimized AlN film.

Chapter 4 presents a detailed study of various parameters of RF sputtering on the aluminum nitride thin films. The study includes the effect of process pressure, process gas composition, and substrate temperature, on deposited film’s properties. The film’s properties are characterized using surface roughness, x-ray diffraction scan, and Young’s modulus analysis. SEM images of the cross-sections of the RF sputtered AlN films are compared with the pulsed DC sputtered films from Chapter 2. This chapter also presents the reflection coefficient and Q-factor of SAW devices fabricated using the RF sputtered film.

In Chapter 5 we present a single beam ion source enhanced magnetron sputtering for producing high-quality ZnTe:N thin films. This chapter presents the optimization of nitrogen flow rate, ion source voltage, and process pressure of the ion source assisted deposition. In this chapter, we also present the comparison of electrical, optical, and structural properties of the ZnTe:N films deposited with and without the ion source.

CHAPTER 2: MAGNETRON SPUTTERING DEPOSITION AND CHARACTERIZATION OF THIN FILMS

2.1. Magnetron Sputtering

Sputtering is a popular vacuum plasma coating process where high-energy particles bombard target material and eject target particles. Figure 2-1 shows a simplified schematic diagram of the magnetron sputtering system. These bombarded target particles then spread around inside the vacuum chamber and some of the target particles land on a substrate placed inside the chamber usually kept in front of the target. The high-energy bombarding particles are positive ions that are created in the vacuum chamber by applying a potential between the target (cathode) and the anode (substrate and chamber wall). To increase the deposition rate of the sputtering process, strong magnets are placed beneath the target to confine the electrons and charged particles of the plasma near the surface of the target. Confining the plasma near the target helps to increase plasma density and deposition rate of the magnetron sputtering process. The widespread use of magnetron sputtering is rooted in its low cost, high deposition rates, excellent coverage of steps and small features, ability to coat heat-sensitive substrates, and so on.

As shown in Figure 2-1, the target is attached to the cathode and is kept at a negative bias voltage. The substrate can be kept floated or electrically connected to the grounded chamber wall, acting as the anode. The chamber is pumped down to a base pressure, typically of the order 10^{-7} - 10^{-6} Torr. Then an inert gas such as argon is fed to the chamber and pressure is raised to a higher pressure, usually some milli-Torrs. Once the electrical power supply is turned on, cosmic radiation-generated electrons are accelerated toward the anode. If the electron gains enough kinetic energy before hitting a neutral argon atom, it can knock out an electron from the argon atom and ionize the argon atoms which follows an avalanche process. In contrast, argon ions also recombine with electrons and form neutral argon atoms. This process keeps going on and reaches equilibrium and a stable plasma discharge is sustained which receives power from the electrical power supply.

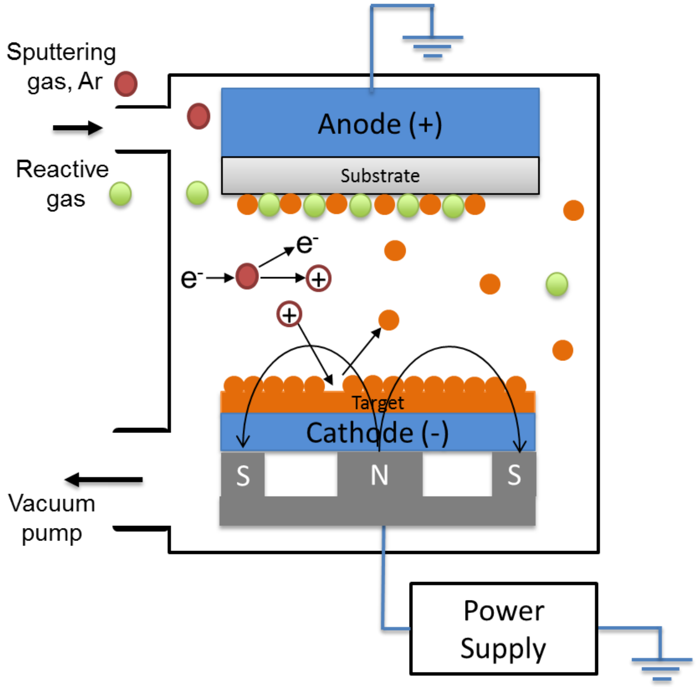

Figure 2-1. Simplified schematic diagram of magnetron sputtering system.

The magnetron acts as a plasma source that houses the target and cathode and utilizes strong electric and magnetic fields to confine charged plasma particles close to the surface of the sputter target. In the presence of the magnetic and electric fields, electrons follow helical paths around magnetic field lines, undergoing more ionizing collisions with gaseous neutrals near the target surface. Plasma-generated Ar^+ ions are accelerated toward the negatively biased target as shown in Figure 2-1. Depending upon the kinetic energy of the positive argon-ion it can bombard the target and (i) get reflected from the target surface, (ii) knock out target atoms/ molecules from the target surface, or (iii) penetrate the target material. Besides, the interaction of the energetic ions with the target surfaces would create a variety of particles such as secondary electrons, neutrals, photons, x-ray, and the implantation of atoms into the substrate. The emitted secondary electron helps to maintain the plasma discharge. The typical kinetic energy of sputtered particles is in the order of 1 - 10 *eV*. This kinetic energy can aid the nucleation and growth processes, increase film density, improve film adhesion, and ease film texturing.

In reactive sputtering, a reactive gas is used which can react with the sputtered particles, and get deposited on the substrate as a compound of the target and the reactive gas element. Most of the reactions between the target material and the reactive gas are believed to occur either on the substrate or the target surface [1,2]. The reactive process occurring at the gas phase is believed to be unlikely as the energy of the compound formation or the kinetic energy of the particles cannot be easily dissipated, resulting in spontaneous dissociation of the compound even if it is formed in the gas phase [2]. The reactive magnetron sputtering process can be used to deposit high-purity films of various alloys and compounds. Magnetron sputtering can be powered by DC, pulsed DC, or RF power supplies as discussed in the following subsequent paragraphs.

2.1.1. DC Magnetron Sputtering (DCMS)

DC magnetron sputtering uses a continuous negative potential applied to the cathode/target of the sputtering system. DC magnetron sputtering system can work well while depositing metal films from a metal target. However, when DCMS is used for reactive sputtering to deposit a compound insulator/ semiconductor film using a metal target, target poisoning and target charge build-up occur. When abundant reactive gas is fed to the plasma chamber, the reactive gas reacts with the target material on the target surface and forms a layer of dielectric. Incoming positive sputtering ions start to accumulate on the dielectric surface, causing dielectric breakdown and arching on the target surface. The formation of a compound on the sputter target results in a significantly reduced sputter yield, thus, reducing the deposition rate. Pulsed DC magnetron sputtering can manage target poisoning and the arching on the target face while maintaining a high deposition rate. The electric field distribution, obtained from a previous simulation, can explain an important aspect of the DC magnetron sputtering [4]. Figure 2-1 shows the electric field distribution along with the distance from the target to the substrate. There can be a strong electric field of around -210 kV/m in the vicinity of the target, which then decreases to zero inside the conducting plasma. The field can get a tiny positive value at the substrate which cannot contribute much to argon ion bombardment on the substrate to densify the film. Besides, the high electric field near the target surface can sputter excessively high-energy target particles which can interrupt the film growth on the substrate.

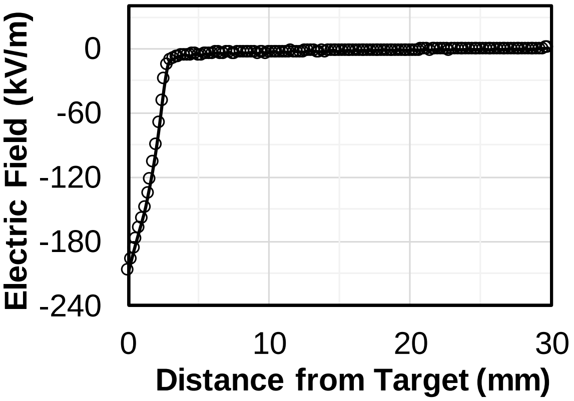

Figure 2-2. Electric field distribution along with the distance from target to the substrate in DC sputtering.

2.1.2. Pulsed DC Magnetron Sputtering

Magnetron sputtering can be powered by a pulsed DC power supply to deposit films of compound materials by reactive sputtering managing arcing and target poisoning. Pulsed DC magnetron sputtering is also very useful for depositing high impedance materials. During a reactive sputtering, the target face can get coated with an insulating layer where consequent positive charge builds up and eventually gets dissipated in the form of arcs. These arcs can cause evaporation of target material droplets which may get deposited on the substrate and result in undesirable film properties and performance.

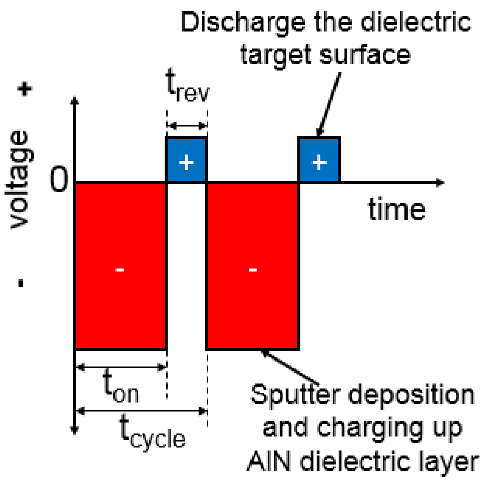

Figure 2-3. The waveform of the target voltage of pulsed DC (asymmetric bipolar) sputtering.

In the pulsed DC sputtering process, a negative bias is applied to the target, having a frequency ranging from a few kHz to several hundred kHz. Between these negative pulses, a positive ‘reverse’ bias is applied to the target to remove any built-up charge on the surface of the target. Figure 2-3 shows such a pulsed DC wave form. The duration of the negative voltage, when the sputtering occurs by bombardments of the positive ion, and positive charge builds up on the target face, is denoted as t_{on}. The short period when the voltage is positive (around +20V) is denoted as t_{rev}. The pulse duty cycle is defined as a ratio of the negative pulse duration (t_{on}) to the pulse period (t_{cycle}). Pulsed DC magnetron sputtering is an arcing-free attractive solution for reactive DC sputtering processes. The average electric potential distribution in pulsed DC is similar to DC due to the large scale in the pulse time.

2.1.3. RF Magnetron Sputtering

RF sputtering is the technique involved in alternating the electrical potential of the target electrode at radio frequencies to avoid a charge building up on insulating sputtering target materials. RF frequency of 13.56 MHz is used internationally for RF sputtering process. The use of the RF power supply can maintain the plasma discharge and avoid the charging of the target surface. In alternating current in RF frequencies, the positive charge does not need to flow through the target, hence working well with the insulator target. If the frequency of the power is less than 50 kHz, the electron and the positive ions in the plasma can respond to the switch of the anode and cathode in alternating half-cycles. But at frequencies above 50 kHz, electrons can move faster than heavier ions. Figure 2-4 shows the graph explanation of the build-up of a negative self-bias of the target. The electron current (I) during the positive half cycle is much higher than the positive ion current (II) during the negative half cycle of the RF voltage. There develops a negative target self-bias (V_c) to make the net current flow zero. This negative target bias, V_c, causes the sputtering to happen. The negative self-bias is typically half the peak-to-peak RF voltage. RF sputtering can produce a very good quality film of any material including insulators or semiconductors. Only a part of the RF power is effectively utilized to sputter the target, making the RF magnetron sputtering deposition rate much slower than DC sputtering.

The electric field distribution, obtained from the previous simulation, can explain the reason why RF sputtering produces denser and smoother film than pulsed DC or DC sputtering [4]. Figure 2-5 shows the electric field distribution along with the distance from the target to the substrate in RF sputtering. Near the substrate, there is an electric field extending up to almost 40 kV/m which can cause some argon ion bombardment on the growing film and improve the film's density and smoothness. Also, the lower electric field near the target surface, unlike the DC sputtering distribution, does not produce excessively high-energy target particles, hence allowing better film growth on the substrate.

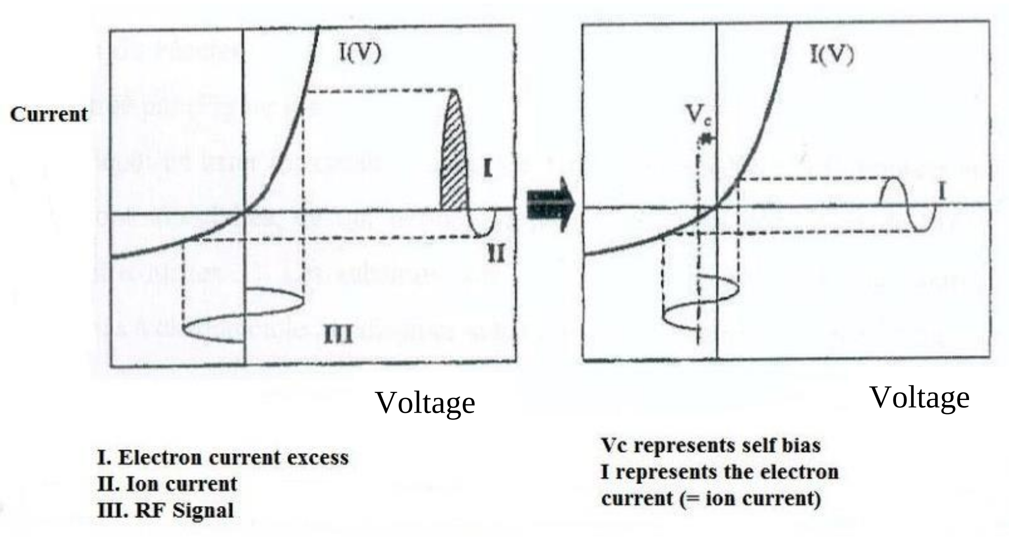

Figure 2-4. Negative self-bias of the target in RF sputtering [7].

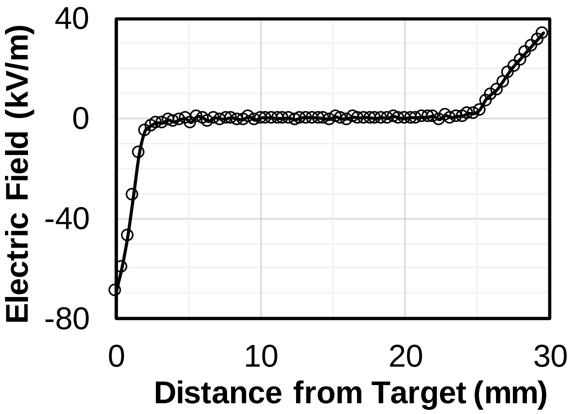

Figure 2-5. Electric field distribution along with the distance from target to the substrate in RF sputtering.

2.1.4. Ion Source Enhanced Magnetron Sputtering

Pulsed DC magnetron sputtering can sputter ceramic and semiconductor materials and offers a *high deposition rate*. However, pulsed DC sputtering involves high (more than 300 V) negative potential applied to the target, hence producing thin films with a rough surface, large crystallites, and poor packing density of the films. RF sputtering process involves lower target bias voltage, hence can produce very high-quality films with a smoother surface and denser film than the pulse DC sputtering. But RF sputtering process suffers from a slow deposition rate. Also, magnetron sputtering at lower pressure usually offers much better films in terms of surface smoothness, film density, and better mechanical & structural properties. However, both pulsed DC and RF magnetron sputtering can operate only above certain pressure levels, usually more than 1 mTorr. Ion source enhanced magnetron sputtering can solve the issues of pulsed DC and RF sputtering and offer modulation of depositing films properties by adjusting the ion source voltage. Ion source enhanced sputtering has been found to sustain plasma at a much lower pressure than pulsed DC and RF sputtering in our experiments.

Ion source enhanced magnetron sputtering uses a single beam ion source in addition to the conventional magnetron. Figure 2-6 shows a photograph and cross-sectional schematic of the single beam ion source. Ion source enhanced pulsed DC magnetron sputtering can offer a high deposition rate as well as a better-quality film than pulsed DC magnetron alone. The additional ion source can help in several ways to improve the process and the deposited film quality. Some of the advantages of this process are as follows:

- the plasma can be sustained at a lower pressure
- the target voltage drops for any fixed power
- ion source provides additional energy to densify the deposited film
- ion source can ionize sputtering/reactive gas
- increased deposition rate
- enhance the doping process in the depositing film

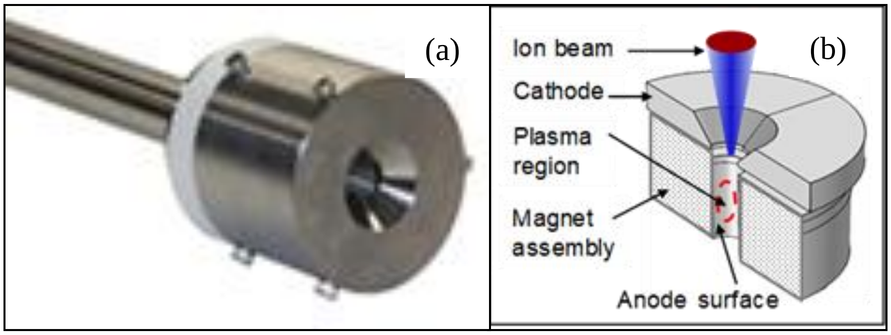

Figure 2-6. (a) Photograph of the single beam ion source and (b) cross-sectional schematic [6].

2.2. Characterization of Thin Films

2.2.1. Laser Acoustic Wave Analysis (LAwave)

Laser acoustic wave analysis (LAwave) is a non-destructive thin film/material surface test device that can determine Young’s modulus, a mechanical property, using surface acoustic waves created by short laser pulses. Figure 2-7 shows a schematic diagram of a LAwave system. The system incident short laser pulses on the sample and makes thermo-elastic excitation which generates the surface acoustic wave on the sample surface. LAwave system detects the surface acoustic wave at a certain distance, thus measuring the wave propagation velocity of the surface acoustic wave. The propagation velocity of the surface acoustic wave is given by Equation (2.1). In the equation, $c, E, v,$ and ρ are the propagation velocity, Young’s modulus, Poisson ration, and material’s density, respectively. The propagation velocity is a function of the Poisson ratio, Young’s modulus, and material density.

$$c = \frac{0.87 + 1.12\, v}{1 + v} \sqrt{\frac{E}{2\rho.(1 + v)}} \tag{2.1}$$

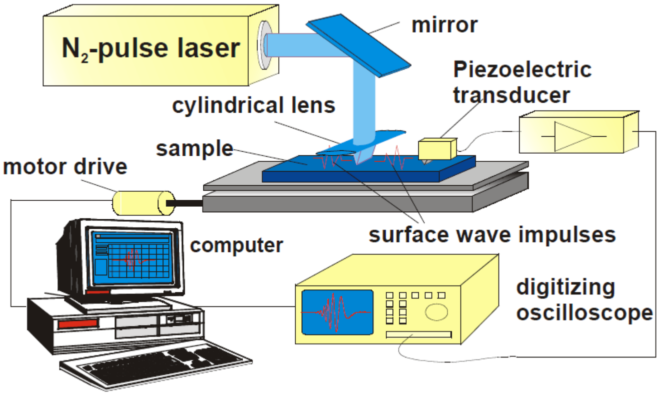

Figure 2-7. Schematic diagram of a Laser Acoustic Surface Wave analysis (LAwave) system [8].

An increase in the frequency of the laser pulse reduces the penetration depth of the wave, so the effect of the film on the surface acoustic wave increases as shown in Figure 2-8. The frequency of the laser pulse/ surface acoustic wave is varied over a wide range and the corresponding propagation velocities are recorded in the system. These frequency-versus-propagation-velocity curves are called *dispersion curves*. The *dispersion curve* depends on the elastic modulus (Young's modulus), density, and thickness of the film. In a case when film material has a higher Young's modulus than the substrate, with an increase in frequency, propagation velocity increases as the acoustic wave propagates mostly in the film. The LAwave system measures the dispersion curve and determines Young's modulus by performing fitting on the measured curve.

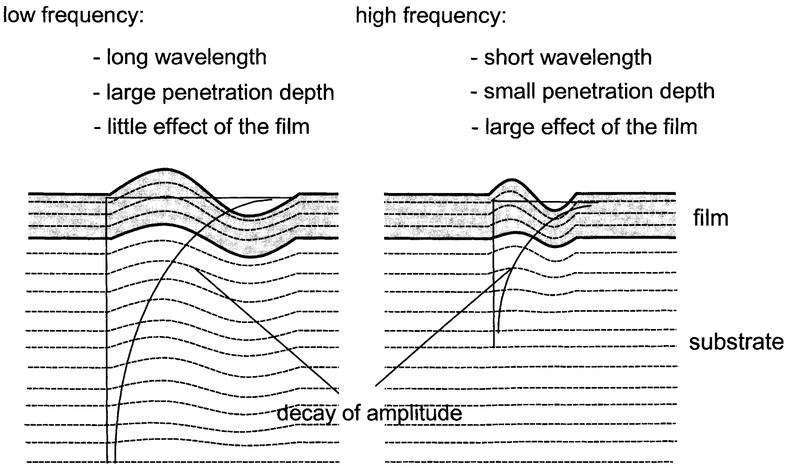

Figure 2-8. Effect of frequency (or wavelength) on the penetration depth of the surface acoustic wave [8]. With an increase in frequency, the effect of film/surface on propagation velocity also increases.

2.2.2. Atomic Force Microscope

An Atomic Force Microscope (AFM) is a high-precision scanning probe microscope that is used in studying samples on the nanoscale. Figure 2-9 shows a schematic diagram of an atomic force microscope. In AFM a tip which is a 3-6 um tall pyramid with a 15-40nm end radius is mounted on a cantilever. The tip is raster-scanned over the sample to get the morphology of the sample. When the tip is brought close to the sample, force (*f*) between the sample and tip causes deflection (*x*) of the cantilever according to Hooke's law,

$$f = -kx \tag{2.2}$$

where, *f*= force between tip and sample, *k* = spring constant of the cantilever, and *x* = deflection of the cantilever. Deflection of the cantilever is detected by an optical arrangement. A laser beam strike is reflected off the back of the cantilever to a segmented photodetector. Whenever the tip moves up and down following the sample surface's morphology, the position of the reflected lased point moves from the setpoint at the photodetector. This information is sent to a computer by a feedback loop to control the z-axis movement of the stage (piezo scanner) to maintain constant separation and force between tip and sample. The sample is moved in the x-y plane to raster scan the desired surface, and corresponding y-axis movement information of the tip is recorded at the computer to construct a three-dimensional morphology of the sample surface. AFM is usually operated in three different operating modes: contact mode, tapping mode, and non-contact mode [9]. This section has been written based on the author's MS thesis "Plasma treatment of zinc oxide thin film and temperature sensing using the zinc oxide thin film" [51].

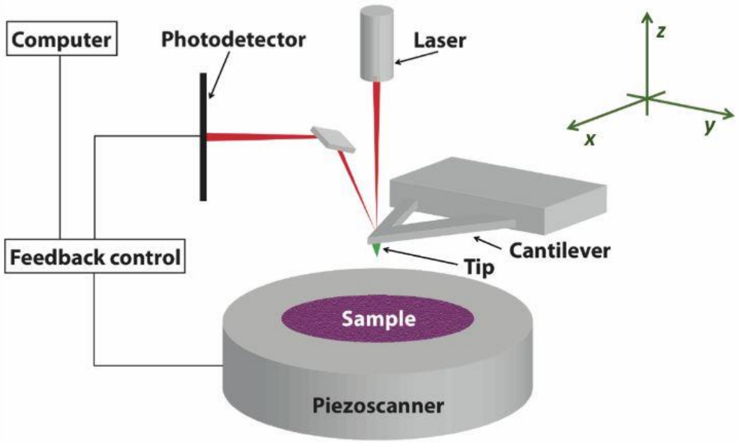

Figure 2-9. Schematic diagram of an atomic force microscope [50].

2.2.3. X-Ray Diffraction Analysis

X-ray diffraction (XRD) is an analytical technique for phase identification of crystalline materials and is used for determining crystal structure, crystallinity, lattice parameters, atomic spacing, and percent phase composition of a sample under test. In XRD X-ray is used as its wavelength is comparable with the spacing of the atomic layers of the crystalline sample. XRD measurements work as a fingerprint of crystalline material. Crystalline materials contain layers of atoms arranged periodically in a specific order. When a monochromatic X-ray beam strikes the sample, the x-ray beam is scattered by atoms in different layers. Such geometry is shown in Figure 2-10. The scattered beam travels in another direction and produces constructive and destructive interference determined by Bragg's law:

$$2d \sin\theta = n\lambda \tag{2.3}$$

here, d is the spacing between diffracting planes, λ is the wavelength of the beam, θ is the incident angle, and n is an integer indicating the order of diffraction.

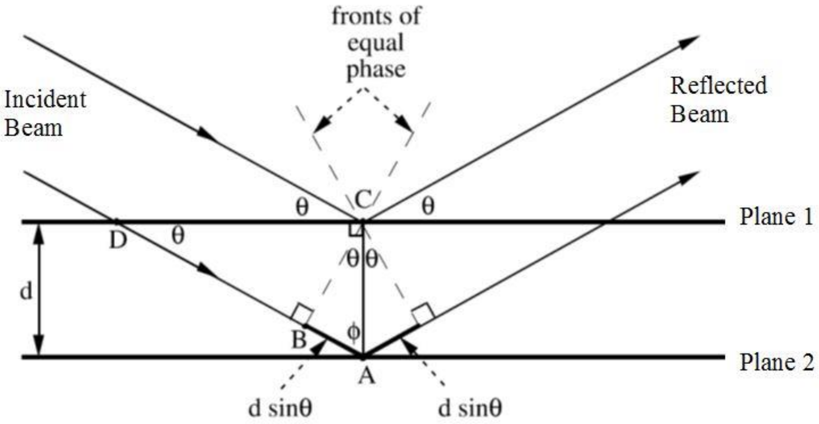

Figure 2-10. The geometry of interference of two waves, scattered by two planes [52].

An X-ray diffractometer is composed of three main components; an X-ray tube, a sample holder, and an X-ray detector as shown in Figure 2-11. X-ray is produced in the X-ray tube by bombarding a metal target with an electron beam emitted from a hot filament. The electron beam knocks out electrons from the K-shell of the target material. Vacancy in the K-shell is filled by an electron dropping down from L or M shell. This dropping electron emits energy in the form of X-rays having a wavelength in the Angstrom range. Copper is the most common target material producing x-ray having a wavelength of 1.5418Å. The X-ray beam is collimated and passed through a monochromator to filter the x-ray beam of a specific wavelength. The monochromatic X-ray beam is then directed to the sample. Incident X-ray interacts with the atomic layers of the sample which scatter the incident beam toward the x-ray detector. X-ray detector detects the scattered beam of X-ray and counts the number of scattered X-rays. The arrangement of detector mounting is such that when the sample is rotated by an angle of θ from the incident beam, the detector mounted on the arm rotates by an angle of 2θ to collect the diffracted X-rays. An instrument named a goniometer is used to maintain the angle and rotate the sample. [52], [53] This section has been written based on the author's MS thesis - "Plasma treatment of zinc oxide thin film and temperature sensing using the zinc oxide thin film" [51].

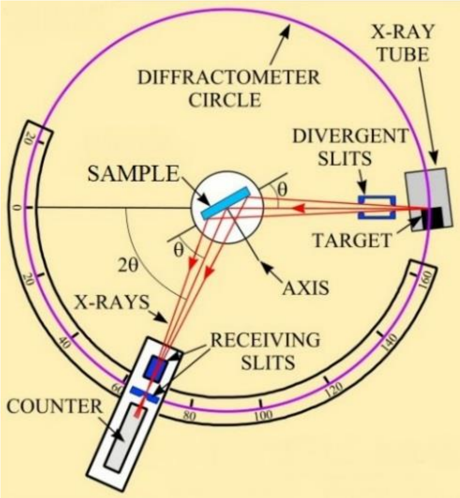

Figure 2-11. Schematic diagram of an X-ray diffractometer [53].

CHAPTER 3: PULSED DC REACTIVE SPUTTERING OF ALUMINUM NITRIDE THIN FILMS

3.1. Introduction

Aluminum nitride (AlN) is a group III-V compound semiconductor having a stable closed packed hexagonal wurtzite structure, as illustrated in Figure 3-1. The hexagonal AlN structure has a lattice parameter of 3.110 – 3.113 Å for the a-axis and 4.978 – 4.982 Å for the c-axis [13]. AlN has a large bandgap (~6.2 eV), good piezoelectric coefficient (d33=5.3 pm/V), very high piezoelectric Curie temperature (~1150 °C) [14], high electrical resistivity (10^{11}–10^{14} Ω cm), high thermal conductivity (320 W/(m.K)), low thermal expansion coefficient (4.2×10^{-6} K^{-1} and 5.3×10^{-6} K^{-1} for the direction along and perpendicular to the c-axis respectively), and excellent chemical stability [15]. AlN has the highest acoustic wave velocity among the piezoelectric materials; 11354 m/s and 5500 m/s for longitudinal and transversal bulk waves respectively, and 5700 m/s for surface waves [3,32]. These properties make AlN an attractive material for applications covering deep ultraviolet (UV) optoelectronics, piezoelectric material for micro-electromechanical systems (MEMS), resonating components in RF-MEMS oscillators, and hard coating [3–6].

Piezoelectric materials with a higher Curie temperature usually have a lower piezoelectric coefficient [2,22,30]. For example, widely used lead zirconium titanate (PZT) has a high piezoelectric coefficient of 410 pC/N but a Cutie temperature of only 250 °C [22]. Aluminum nitride (AlN), an attractive piezoelectric material, can operate at a very high temperature of around 1150 °C and possess a reasonable piezoelectric coefficient of 5.5 pC/N [14].

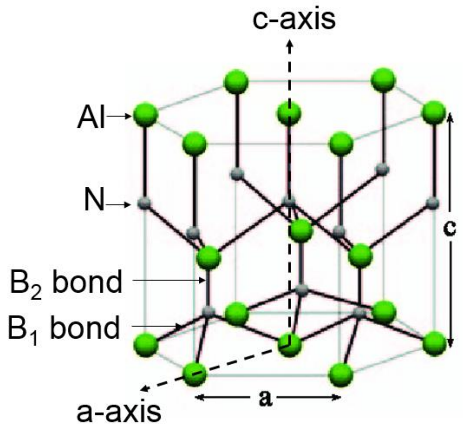

Figure 3-1. Hexagonal wurtzite crystal structure of aluminum nitride. Each Al atom coordinates four N atoms and vice versa. B_1 bond length is 1.885 Å and B_2 bond length is 1.917 Å [23].

AlN thin films can be grown by various methods, including chemical vapor deposition [12,13], molecular beam epitaxy [14], pulsed laser deposition [15], and magnetron sputtering [1]. Magnetron sputtering is advantageous for being a low-temperature and low-cost process [1]. Magnetron sputtering can be operated by an RF or a pulsed DC power supply. Pulsed DC magnetron sputtering offers the advantage of higher deposition rates than RF [16,17]. When sputtering from a metallic Al target with argon and nitrogen as process gas, it is termed reactive sputtering deposition. During reactive sputtering, sputtered Al atoms react with nitrogen gas and form an AlN film on the substrate. To achieve the desired structural and morphological, optimization of deposition parameters is essential.

A surface acoustic wave (SAW) device is often used to demonstrate the piezoelectric properties of AlN thin films. Figure 3-2 shows a schematic diagram of a SAW device. SAW devices are seeking the attention of researchers for their widespread applications in sensors and wireless communications [33–39]. To increase sensitivity and to enable the use of SAW devices in high-frequency wireless communications, a high operating frequency of SAW devices is required. The operating frequency of a SAW device can be increased by miniaturizing the dimension of interdigital transducer (IDT) electrodes. But miniaturization of IDT dimensions is limited by photolithography and the etching process [35,39–42]. The operating frequency of a SAW device can also be increased by choosing a piezoelectric material with higher acoustic wave velocity. AlN has the highest acoustic velocity among piezoelectric materials [37–39]. AlN (002) film, with the c-axis perpendicular to the surface, and a very smooth surface, are required for the best SAW device performance [16,30,31,40].

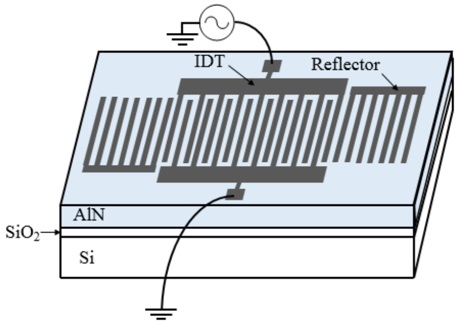

Figure 3-2. Schematic diagram of a SAW device.

Despite the extensive research on AlN film processes, there is a gap in comprehensive studies on the effects of pulse parameters on the structure and properties of pulsed DC reactive sputtered AlN films. The pulse parameters are expected to greatly affect the resulting film structure and properties because they can modulate the average ion kinetic energy. Another aspect of this research is, that we characterize an important mechanical property – Young's modulus of the deposited films. So, this work reports a systematic and comprehensive optimization of common process parameters, including pulse parameters, on the structure and properties, including Young's modulus, of pulsed DC sputtered AlN films.

In this chapter, we present the process-parameter optimization of [002] oriented AlN thin films. Process pressure and nitrogen concentration have the most significant influence on the topography and morphology of the film, deposited by the pulsed DC reactive sputtering method.

DC pulse parameters such as pulse frequency and pulse duty cycle also influence the properties of deposited AlN films, which have been reported in this work. This work addresses the influences of process and pulse parameters on Young's modulus besides other characteristic properties of the film.

This chapter is written based on a manuscript accepted for publication in *Thin Solid Films* titled, "*Pulsed direct-current reactive sputtering of high Young's modulus [002] oriented aluminum nitride thin films*", by AA. Talukder, *et al*.

3.2. Previous Works

Depending on the intended use, various growth methods, including chemical vapor deposition, molecular beam epitaxy, pulsed laser deposition, and magnetron sputtering, have been utilized to fabricate AlN thin films [21,24–27,41–49]. Among all these methods, magnetron sputtering is very advantageous for its simplicity, low cost, low thermal budget, and widespread availability, allowing the growth of AlN films with controllable properties [1,14,15,43].

Magnetron sputtering of AlN films can be done from a metallic Al or a ceramic AlN target. While sputtering from a metallic Al target, reactive gas nitrogen is added to the sputtering argon gas, and the method is known as a reactive sputtering method. The reactive sputtering method can use either a radio frequency (RF) or a pulsed direct current (DC) power supply. The use of pulsed DC reactive sputtering can offer a high deposition rate and better control over the deposition process [17,18,28,29,41,48,50].

Numerous studies have been carried out on the fabrication of c-axis oriented AlN thin films deposited by DC reactive sputtering technique from an Al target [1,16–18,20,21,24,43]. The influence of common process parameters such as substrate temperature, gas pressure, nitrogen concentration, substrate type, and magnetron power on the properties of DC reactive sputtered AlN films have been investigated in various studies [9,18–27].

Kar *et al.* reported their study on a reactive DC sputtering deposition of AlN thin films from a metallic Al target. They inspected the influence of deposition temperature and nitrogen gas content on electrical and morphological properties such as crystal orientation, bond formation, surface roughness, and grain size of the reactively sputtered AlN films. An increase in temperature was found to be associated with increased surface roughness and grain size. Higher nitrogen concentration resulted in a smaller grain size and a smoother surface of the reactively sputtered film [45,46].

Four other papers by Cheng *et al.*, Chiu *et al.*, Iborra *et al.*, and Dubois *et al.* reported the influence of process parameters such as pressure, sputtering power, and substrate bias on the preferred orientation, grain size, residual stress and piezoelectric coefficients of reactive sputtered AlN films [19–21,34].

Ababneh *et al.* have reported the effect of process pressure, process gas composition, and plasma power on the c-axis orientation and bi-axis stress level of reactive DC sputtering of piezoelectric AlN thin films from a metallic Al target. C-axis orientation of the film was reported for elevated nitrogen concentration and decreased sputtering pressure. However, the influence of plasma power on the microstructure of the reactive DC sputtered film was found to be negligible [35].

Yang *et al.* reported reactive sputtering deposition of AlN films from a metallic Al target and fabrication of SAW resonators utilizing the AlN films. They studied the impact of various device parameters such as IDT finger spacing, IDT finger aperture, reflector types, number of reflector gratings on the SAW device performance [31].

Besides these common process parameters, DC pulse parameters such as pulse frequency and pulse duty cycle can also affect the morphology and structure of a reactively sputtered film [28]. Cherng et al. reported a study of the effect of pulse parameters such as reverse voltage, pulse frequency, and pulse duration on the crystalline property of reactively sputtered AlN films through XRD analysis [28]. An increase in reverse voltage resulted in a detrimental effect on [002] orientation of the AlN film, whereas an increase in pulse frequency within the range of 10 kHz to 50 kHz improved the c-axis orientation of the AlN film [28].

Another study by Kohout et al. reported a reactive low duty cycle magnetron sputtering deposition of [002] oriented AlN films [6]. The authors optimized deposition conditions such as reactive gas flow, working pressure, average target power, substrate temperature, substrate bias, and the level of target erosion. The optimized AlN films had a hardness of 22 GPa and residual stress of around 300 MPa [6].

Commonly explored process parameters of magnetron sputtering of AlN are, substrate temperature, process pressure, gas composition, substrate type, and pulse parameters. Most of the research reported studies on a single process parameter in each paper. Therefore, there is a lack of a comprehensive study on all these important parameters and requires an investigation of how the films' properties can be systematically optimized, which has been addressed in this chapter.

3.3. Experimental Procedures

3.3.1. AlN Film Deposition and Characterization

Silicon substrates (1”x1”) were prepared by cleaving (100) silicon wafers. The substrates were then cleaned ultrasonically in acetone and methanol in sequence for ten minutes in each solvent. Then the substrates were blow-dried using a nitrogen gas gun. A sputtering deposition system (Kurt J. Lesker Company® PRO Line PVD 75) having three Torus magnetron sputtering sources and equipped with a pulsed DC power supply was used for the deposition of AlN films. Table 3-1 enlists the parameters of the pulsed DC sputtering process.

Table 3-1. Parameters of the pulsed DC sputtering process.

Target	Ø3” Aluminum (99.99% pure)
Substrate	(100) silicon (1” × 1”)
Substrate temperature	300 °C
Sputtering power	250 W (pulsed DC)
Pulse frequency	25 kHz – 300 kHz
Pulse duty cycle	70% - 90 %
Deposition time	45-90 minutes
Film thickness	200-350 nm
Process gas	Argon (Ar) and Nitrogen (N2)
Base pressure	2 x 10-7 Torr
Process pressure	1 mTorr – 5 mTorr
Target to substrate distance	5.5 inches
Substrate rotation speed	10 revs/min
Temperature ramp up/down	10 °C/min
Magnetron ramp up/down	0.2 Watt/sec

Table 3-2 shows the parameters for optimizing the pulsed DC reactive sputtering. The equipment includes a standalone real-time controller for the automatic process. All the process parameters, i.e., substrate temperature, process gas flow rate, DC power level, DC pulse frequency, and DC pulse duty cycle, were controlled and monitored using an interface software program. Though the target voltage is a negative potential relative to the chamber wall, the only magnitude of the target voltage has been used in the following graphs for simplicity. The magnitude of the positive *reverse* voltage was set to be 20% of the negative *ON* voltage. Resistive-electric heaters were used to heat the substrate and maintain it at the desired temperature. After preliminary temperature studies, the substrate temperature was maintained at 300°C for all the depositions.

Table 3-2. Parameters for process optimization of the pulsed DC reactive sputtering.

Study parameter	Pressure (mTorr)	N2 gas content (%)	Pulse frequency (kHz)	Pulse duty cycle (%)
Process pressure	varying: 1, 3, 5	50	50	75
Process gas composition	1	varying: 50, 75, 100	50	75
Pulse frequency	1	100	varying: 25, 50, 100, 200, 300	80
Pulse duty cycle	1	100	100	varying: 70, 80, 90

XRD measurements of the AlN films were carried out using a *Rigaku SmartLab* XRD system with Cu-Kα radiation (λ=1.54 Å). Surface topography and surface roughness (R_q) of the films were characterized using a *Hitachi AFM5100N* scanning probe microscope (SPM) with *μmasch's HQ:NSC14/Al* tips (tip radius: 8 nm, tip height: 12-18 μm, tip cone angle: 40°, resonance frequency: 160 kHz, force constant: 5 N/m) along with *Gwyddion* SPM data analysis software. While evaluating surface roughness (R_q) from the 2 μm × 2 μm SPM image, three scan lines each having lengths of 1.8 μm and a waviness cutoff wavelength of 257 nm were used. A *LAwave®* (laser acoustic wave) system was used for determining Young's modulus of the AlN films [30]. Cross-sectional image of 1 μm thick AlN film was taken using an ultra-high resolution JEOL 7500F field emission scanning electron microscope.

3.3.2. SAW Device Fabrication and Characterization

Silicon wafers of 3” diameter were used for making SAW devices. The wafers were cleaned with acetone and methanol, then blow-dried using a nitrogen gas gun. Then Kurt J. Lesker Company® PRO Line PVD 75 deposition system was used to sputter deposit SiO_2, AlN, and Al layers on the wafer. The deposition parameters of these layers are listed in Table 3-3. The top aluminum layer was patterned to obtain the IDT electrode using a photomask and aluminum etchant. Surface acoustic device chips were diced using an *ADT 7120* wafer dicing saw machine. Individual SAW chips were mounted on a printed circuit board (PCB), and wire bonded to an SMA connector mounted on the edge of the PCB. A network analyzer (300 kHz – 3 GHz, *Agilent Technologies*) was used to determine the scattering parameter, S_{11} of the devices.

Table 3-3. Sputtering process parameters of different layers of the SAW device.

Film (layer)	**SiO2 (bottom)**	**AlN (middle)**	**Al (top)**
Pressure	5 mTorr	1 mTorr	4.5 mTorr
Temperature	200 °C	300 °C	25 °C
Power	200 W (rf, 13.56 MHz)	250 W (pulsed DC, f: 100 kHz, duty cycle: 80%)	100 W (pulse dc, f: 50 kHz, duty cycle: 75%)
Target	SiO2	Al	Al
Substrate	Si (100)	SiO2/Si	AlN/SiO2/Si
Process gas	Ar	100% N2	Ar
Thickness	500 nm	1 µm	150 nm

3.4. Results and Analysis

3.4.1. Effect of Process Pressure

The process pressure was found to significantly influence the discharge voltage and current, as illustrated in Figure 3-3, in the pulsed DC reactive sputtering of AlN. The target voltage decreased sharply as the process pressure increased from 1 mTorr to 3 mTorr. As the pressure further increases to above 3 mTorr, the voltage only varied slightly. With the pulsed DC power fixed at 250 W, the discharge current had a tendency opposite to the target voltage; the current increased with the increase in the process pressure. At lower pressure, there were fewer ions, causing lower discharge current, which resulted in a higher target voltage for a fixed power supplied to the magnetron. Figure 3-4 shows the variation in deposition rates with process pressure of the pulsed DC reactive sputtering of AlN. With an increase in pressure, the deposition rates went down, which is attributed to background gas scattering.

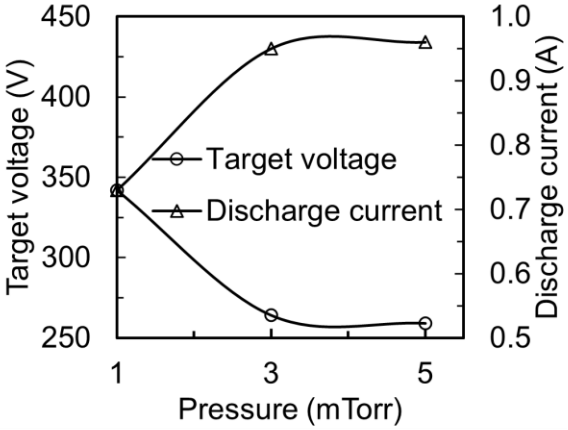

Figure 3-3. Variation of target voltage and discharge current with process pressure of the pulsed DC reactive sputtering of AlN.

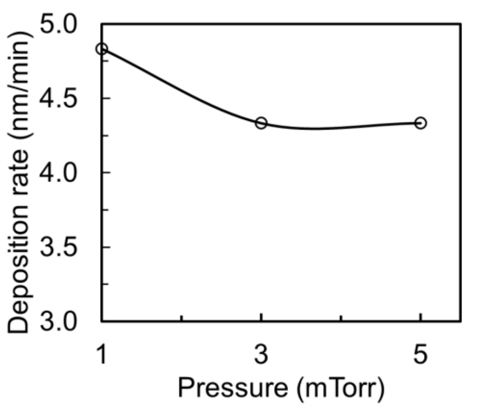

Figure 3-4. Variation in deposition rates with process pressure of the pulsed DC reactive sputtering of AlN.

The process pressure had a significant influence on the topography of the deposited AlN films. Figure 3-5 shows the roughness values of AlN films deposited at various process pressures. The roughness of the films continued to decrease with lowering the deposition pressure. AlN films deposited at 1 mTorr had RMS roughness of only 1.8 nm. Any further lowering of the chamber pressure was not a viable choice, as the plasma became unstable at pressure levels lower than 1 mTorr while maintaining the pulsed DC power at 250 watts. At lower pressure, the sputtered atoms experience fewer collisions before reaching the substrate. Hence, they possess higher kinetic energy, enabling better surface diffusion and coalescence, which result in a smoother film surface. Figure 3-6 shows the XRD pattern of AlN films deposited by pulsed DC reactive sputtering at various process pressures. FWHM for films deposited at 5 mTorr, 3 mTorr, and 1 mTorr process pressure were 0.49°, 0.47°, and 0.40°, respectively. The process pressure had a significant influence on the film microstructure. Highly [002] oriented film was achieved when deposited at a pressure of 1 mTorr. At higher process pressures, e.g., 3 mTorr and 5 mTorr, the (002) peak intensity and sharpness were much lower. AlN film deposited at 5 mTorr pressure showed a weak (101) peak. With the reduction in the process pressure, the (101) peak continued to decrease and vanished at 1 mTorr. At low process pressure, the deposited atoms have high kinetic energy, which could reorder and reassemble on the substrate surface to crystallize in [002] direction.

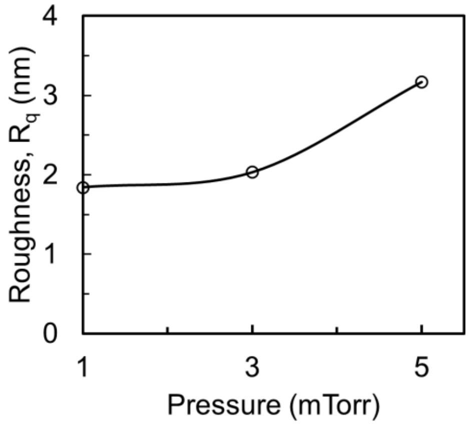

Figure 3-5. Roughness values of AlN films deposited by pulsed DC reactive sputtering at various process pressures.

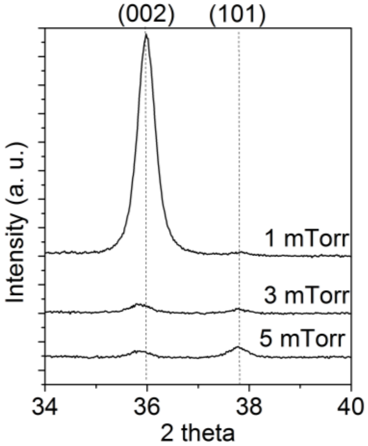

Figure 3-6. XRD pattern of AlN films deposited by pulsed DC reactive sputtering at various process pressures.

The process pressure also influenced Young’s modulus of the pulsed DC reactive sputtered AlN films. Figure 3-7 shows Young’s modulus values of AlN films deposited by DC reactive sputtering at various process pressures. Films deposited at lower process pressure exhibited higher Young’s modulus. This result is very much correlative with XRD data. Films deposited at lower pressure showed better crystallinity and [002] orientation, resulting in denser films with higher

Young's modulus. AlN film deposited at 1 mTorr had Young's modulus of 312 GPa. Moreover, the discharge voltage had a secondary effect on the film crystallinity, surface roughness, and Young's modulus. Higher target voltage leads to more energetic depositing species, thus denser film with higher Young's modulus, better crystallinity, and lower surface roughness. As a result, Young's modulus (Figure 3-7) and XRD peaks sharpness (Figure 3-6) follow the variation in the target voltage (Figure 3-3), while the surface roughness (Figure 3-5) follows an opposite trend to the target voltage.

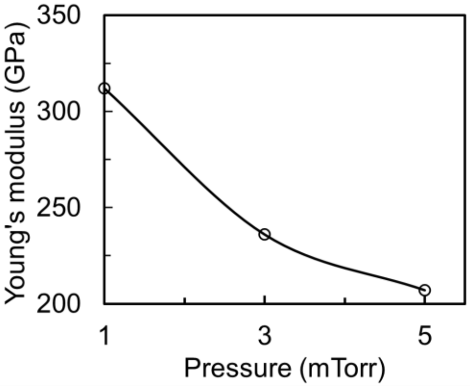

Figure 3-7. Young's modulus values of AlN films deposited by DC reactive sputtering at various pressures.

3.4.2. Effect of Process Gas Composition

The Ar-N_2 process gas composition influenced the discharge voltage-current characteristics of the pulsed DC reactive sputtering of AlN. Figure 3-8 shows the variation of target voltage and discharge current with the nitrogen content of the pulsed DC reactive sputtering of AlN. With an increase in nitrogen gas content, the discharge current decreased slowly to 75% and rapidly from 75% to 100%. As nitrogen ionizes less efficiently than argon, the plasma density would be reduced with higher nitrogen content, which resulted in a lower discharge current [31,32]. With fixed target power, the target voltage curve varied in an opposite trend of the discharge current. Figure 3-9 shows the variation of deposition rate with nitrogen content in the pulsed DC reactive sputtering of AlN. Both the variation in target voltage and the presence of lighter N^+ sputtering species affected the deposition rate. The deposition rate plummeted as the nitrogen content was increased from 50% to 75%. When the nitrogen content varied from 50% to 75%, the target voltage was almost the same, as seen in Figure 3-8. However, with 75% nitrogen content, the deposition rate was much lower than that at 50% nitrogen, as nitrogen is much lighter than argon, hence resulting in a much lower sputtering yield and deposition rate. As nitrogen content brought from 75% up to 100%, the significant increase in target voltage increased the ions' kinetic energy and higher sputtering yield. The higher sputtering yield could increase the deposition rate slightly at 100% nitrogen content.

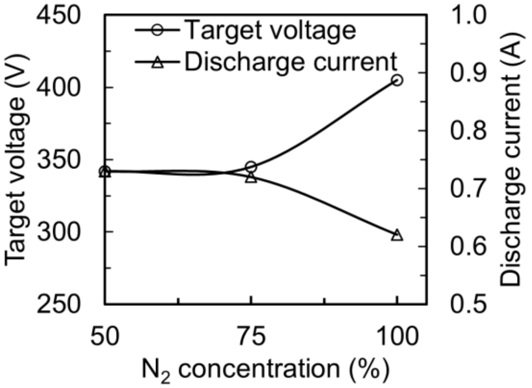

Figure 3-8. Variation of target voltage and discharge current with the nitrogen content of the pulsed DC reactive sputtering of AlN.

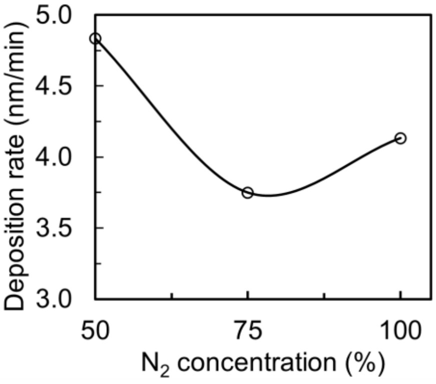

Figure 3-9. Variation of deposition rate with the nitrogen content of the pulsed DC reactive sputtering of AlN.

It is necessary to add nitrogen gas to the process gas to form AlN films from a metallic aluminum target, so sputtered aluminum could react with nitrogen and form aluminum nitride. Preliminary studies on the nitrogen gas content revealed that at least 50 % nitrogen was needed to deposit stoichiometric films with crystal growth in [002] orientation. Figure 3-10 shows the XRD pattern of AlN films deposited by DC reactive sputtering with various nitrogen gas contents. FWHM for films deposited with 50 %, 75 %, and 100 % nitrogen gas were 0.4044°, 0.3852°, and 0.3240°, respectively. Continued decrease in FWHM values with the increase in nitrogen gas content in process gas mixture refers to better [002] crystal orientation. With an increased nitrogen gas content, the intensity of the (002) peak increased but did not appear to influence the stoichiometry anymore. For higher nitrogen gas content, collision with lighter nitrogen plasma species in the background would result in less loss in the kinetic energy of the depositing molecules. Also, higher nitrogen gas content resulted in higher target voltage, as seen in Figure 3-8, which caused a stronger bombardment of sputtering N^+ on target and ejected energetic AlN molecules/species. These depositing molecules with higher energy would be favorable for better surface diffusion, thus making larger crystallite clusters and better crystallinity.

The influence of N_2 gas content on the surface roughness of the deposited AlN films was found to be less significant. Figure 3-11 shows the roughness values of the AlN films deposited with pulsed DC reactive sputtering at various nitrogen gas contents. The roughness of the film initially increased with the increase in nitrogen content from 50% to 75%, and then the roughness declined slightly as the nitrogen content was increased to 100%. The first increase in roughness could be attributed to the significant increase in crystallite size, which made the film’s surface rougher. But a further increase in nitrogen content beyond 75% nitrogen gas content reduced the roughness slightly. This could be attributed to the significant increase in target voltage with nitrogen content higher than 75%, as seen in Figure 3-8, which could favor densification and surface-smoothening of the film.

Figure 3-12 shows Young's modulus values of AlN films deposited at various nitrogen gas contents. The variation of N_2 gas content did not appear to influence Young's modulus of the deposited AlN films significantly. The first decrease in Young's modulus from 50% to 75% nitrogen gas content could be attributed to the formation of larger crystallites at higher nitrogen content. With larger crystallites, the grain boundaries would be more inconsistent and defective, thus lowering the effective density and Young's modulus of the film. However, with nitrogen content higher than 75%, there was a substantial increase in the target voltage, as seen in Figure 3-8. That increased target voltage could favor the film's densification and improve Young's modulus of the grown film.

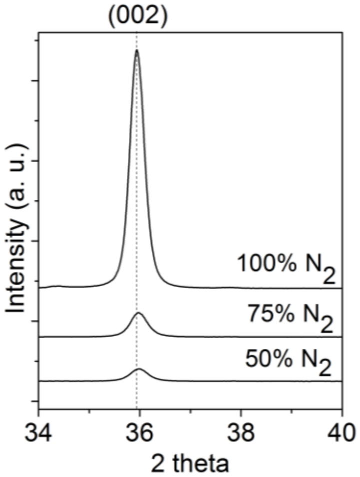

Figure 3-10. XRD pattern of AlN films deposited by DC reactive sputtering with various nitrogen gas contents.

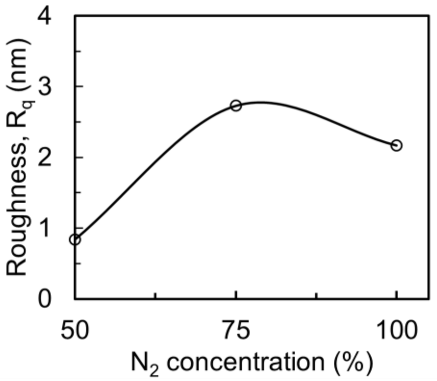

Figure 3-11. Roughness values of AlN films deposited by DC reactive sputtering at various nitrogen gas contents.

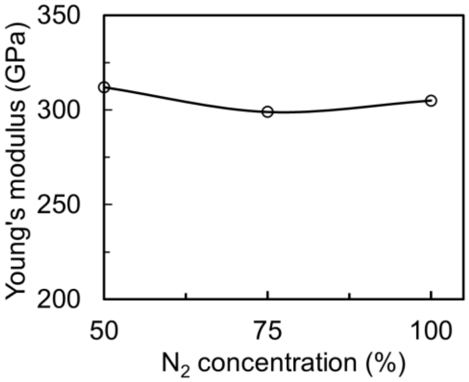

Figure 3-12. Young’s modulus values of AlN films deposited by DC reactive sputtering at various nitrogen gas contents.

3.4.3. Effect of Pulse Frequency

Pulse frequency could influence the target voltage and discharge current of the pulsed DC reactive sputtering process. Figure 3-13 shows the variation of target voltage and discharge current with the pulse frequency. 100-200 kHz resulted in maximum target voltage and consequently the minimum discharge current. Above 200 kHz, the reverse time (t_{rev}) is squeezed too much to completely discharge the accumulated positive charge on the poisoned or nitrided target surface during the previous “active sputtering time” or “on” time (t_{on}). This insufficient discharging of the nitrided target surface resulted in a reduced (negative) potential of the target at a higher pulse frequency at 300 kHz. On the other hand, at a lower frequency below 100 kHz, the “on” time of the pulse is too long that the nitrided target surface accumulates too much positive charge during "on" or "active sputtering time". This higher level of positive charge accumulation causes the effective negative potential of the target to drop at lower frequencies.

In the frequency study, the deposition rate is solely dictated by the target voltage. Figure 3-14 shows the variation of deposition rate with the pulse frequency of the pulsed DC reactive sputtering of AlN. The deposition rate varied correspondingly with the target voltage as sputtering ion species are fixed at 100% nitrogen. Higher deposition voltage caused higher sputtering yield and vice versa.

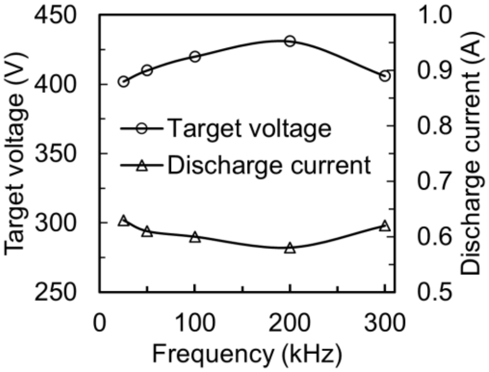

Figure 3-13. Variation of target voltage and discharge current with the pulse frequency of the pulsed DC reactive sputtering of AlN.

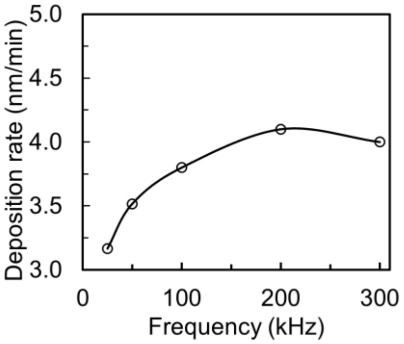

Figure 3-14. Variation of deposition rate with the pulse frequency of the pulsed DC reactive sputtering of AlN.

Pulse frequency can influence the topographical and morphological properties of the AlN films. Figure 3-15 shows the XRD 2-theta curves of AlN films deposited by pulsed DC reactive sputtering with various pulse frequencies. The deposited films have preferred [002] orientation for all frequencies. The FWHMs are 0.46°, 0.45°, 0.42°, 0.43°, and 0.44° for 25 kHz, 50 kHz, 100 kHz, 200 kHz, and 300 kHz, respectively. The film deposited with 100 kHz pulse frequency had the lowest FWHM value indicating the strongest [002] orientation for 100 kHz pulse frequency. However, as the FWHM values of the 2-theta scans are very close for 50 kHz, 100 kHz, and 200 kHz, rocking curve data can confirm the relative differences among films deposited with these pulse frequencies. Figure 3-16 shows the XRD rocking curve of AlN films deposited with various DC pulse frequencies. The FWHM values are 5.71°, 4.61°, and 4.82° for pulse frequencies of 50 kHz, 100 kHz, and 200 kHz, respectively. The rocking curve data reveals the best crystal quality for 100 kHz with no noticeable peak shift and the lowest FWHM values among the films deposited with pulse frequencies of 50-200 kHz.

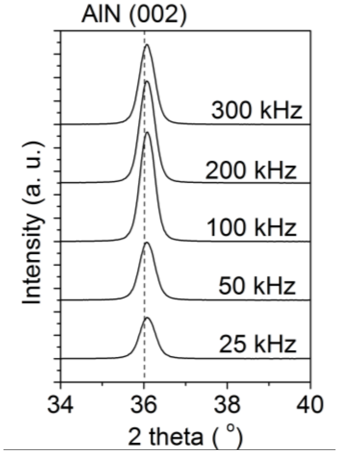

Figure 3-15. XRD 2-theta curves of AlN films deposited with various DC pulse frequencies.

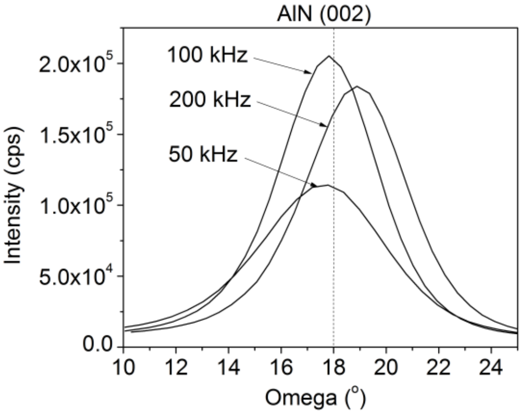

Figure 3-16. XRD rocking curve of AlN films deposited with various DC pulse frequencies. The FWHM values are 5.71°, 4.61°, and 4.82° for pulse frequencies of 50 kHz, 100 kHz, and 200 kHz, respectively.

Figure 3-17 shows the roughness values of AlN films deposited by DC reactive sputtering with various pulse frequencies. Films deposited at a pulse frequency of 100 kHz and 200 kHz had the lowest similar minimal roughness. Figure 3-18 shows Young's modulus values of AlN films deposited by DC reactive sputtering with various pulse frequencies. Young's modulus data correlates with the roughness data, i.e., the highest Young's modulus was obtained for 100 and 200 kHz with a value around 335 GPa. There are more on-off cycles with 100 kHz than 25 kHz or 50 kHz within a specific time for a fixed duty cycle. That led to more frequent refreshing of the target surface and, additionally, shorter periods of on-time, i.e., the negative potential and active sputtering time, at 100 kHz, which also offers less accumulation of positive N+ charge on nitrided target. The result was a homogeneous film with fewer defects. However, at a higher frequency beyond 200 kHz, the discharging reverse time is squeezed to a minimal value, which might not be enough to discharge the nitrided target surface, resulting in a decline in topographical and morphological properties of the deposited films. A higher target voltage favors the densification, crystallization, and surface-smoothening of the depositing film. Therefore, Young's modulus (in Figure 3-18) and XRD peak sharpness (Figure 3-15) follow the target voltage profile (in Figure

3-13), and the surface roughness profile (in Figure 3-17) follows an opposite trend to the target voltage profile.

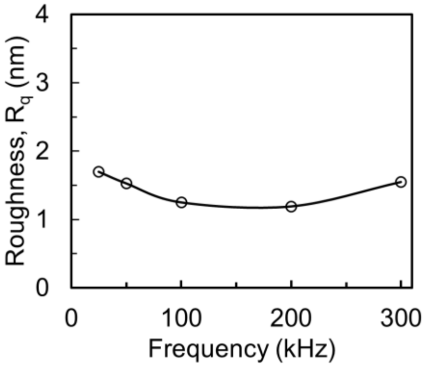

Figure 3-17. Roughness values of AlN films deposited by DC reactive sputtering with various pulse frequencies.

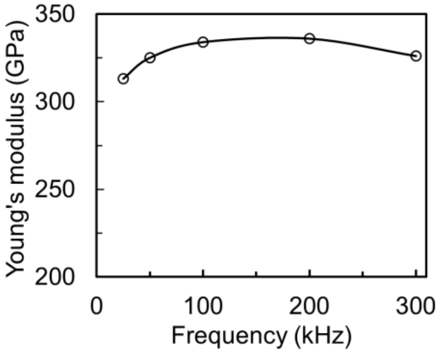

Figure 3-18. Young’s modulus values of AlN films deposited by DC reactive sputtering with various pulse frequencies.

3.4.4. Effect of Pulse Duty Cycle

Variation in pulse duty cycle affects target voltage and discharge current. Figure 3-19 shows the variation of target voltage and discharge current of the pulsed DC reactive sputtering deposition of AlN. A pulse duty cycle of 80% offered the highest target voltage; thus, the lowest discharge current, which can be attributed to the balanced charge build-up during “on” time (t_{on}) and discharging during the reverse time (t_{rev}) of the nitrided target. Figure 3-20 shows the variation of the deposition rate of the pulsed DC reactive sputtering deposition of AlN. The deposition rate variation follows the variation profile of the target voltage in Figure 3-19, which confirms the higher sputtering yield at a higher voltage and vice versa.

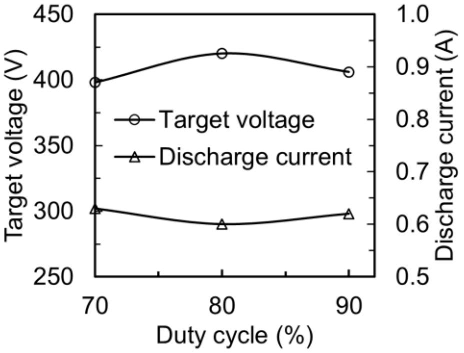

Figure 3-19. Variation of target voltage and discharge current of the pulsed DC reactive sputtering deposition of AlN.

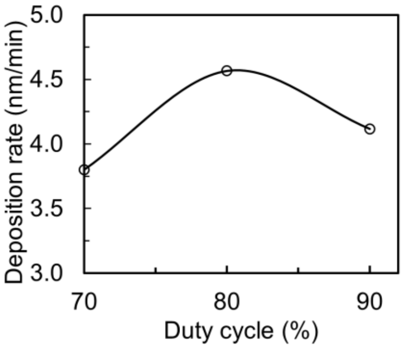

Figure 3-20. Variation of the deposition rate of the pulsed DC reactive sputtering deposition of AlN.

The duty cycle of the DC pulse was observed to influence the properties of the AlN films slightly. Figure 3-21 shows the XRD pattern of AlN films deposited by pulsed DC reactive sputtering with different duty cycles at a DC pulse frequency of 100 kHz. The FWHMs are 0.44°, 0.42°, and 0.45° for 70 %, 80%, and 90% duty cycle, respectively. The lowest FWHM for the (002) peak was found for the sample deposited with a duty cycle of 80%. The occurrence of the lowest FWHM for the 80% duty cycle can be attributed to the highest target voltage, as seen in Figure 3-19, which resulted in depositing AlN atoms with the highest energy at that duty cycle.

Figure 3-22 shows the roughness values of AlN films deposited by pulsed DC reactive sputtering with various pulse duty cycles. The lowest roughness was achieved for the film deposited with the DC pulse duty cycle of 80%. Figure 3-23 shows Young's modulus of AlN films deposited by pulsed DC reactive sputtering with various duty cycles. The highest Young's modulus of 335 GPa was achieved for the film deposited with the pulse duty cycle of 80%. For a duty cycle of 80%, which offered the highest target voltage, the film grew efficiently with better crystallinity, higher density, and lower roughness. The same explanation can be applied to Young's modulus. A duty cycle of 80% at a frequency of 100 kHz was found to be the most optimum pulse parameter.

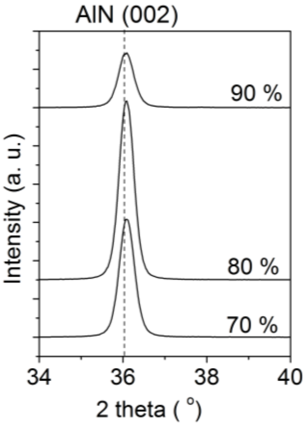

Figure 3-21. XRD pattern of AlN films deposited by pulsed DC reactive sputtering with different duty cycles.

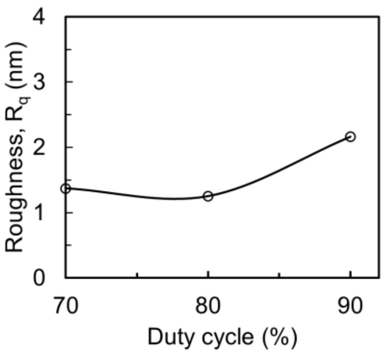

Figure 3-22. Roughness values of AlN films deposited by pulsed DC reactive sputtering with various pulse duty cycles.

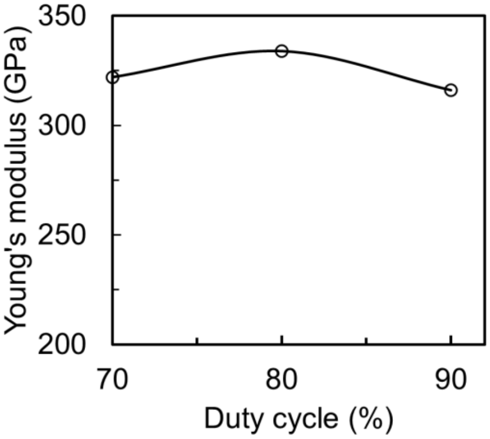

Figure 3-23. Young's modulus of AlN films deposited by pulsed DC reactive sputtering with various duty cycles.

3.4.5. Properties of 1 µm Thick AlN Film

A scanning electron microscope (SEM) image of the film's cross-section can provide vital information about the nature of film growth. For understanding the film's growth, a thick film is required. AlN film of 1 µm thickness was deposited with optimized process parameters: 1 mTorr process pressure, 100% N_2 concentration, 100 kHz pulse frequency, and 80% pulse duty cycle. Figure 3-24 shows the SEM cross-sectional image of 1 µm thick pulsed DC reactive sputtered AlN film deposited with optimized conditions. Columnar growth of the AlN film can be observed from the SEM cross-sectional image. As the film grew thicker (in the vertical direction), the crystallites became larger. Figure 3-25shows the AFM topography image of the 1 µm thick AlN film deposited with optimized conditions. RMS roughness of the 1 µm thick film was measured to be 3.94 nm, which is higher than the previous samples, deposited for process-parameter optimizations. As the film grew thicker, crystallites became larger, which resulted in a rougher surface.

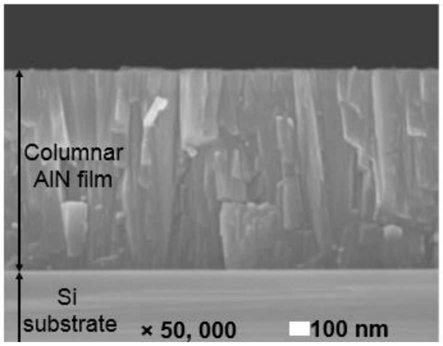

Figure 3-24. SEM cross-sectional image of 1 µm thick pulsed DC reactive sputtered AlN film deposited with optimized conditions.

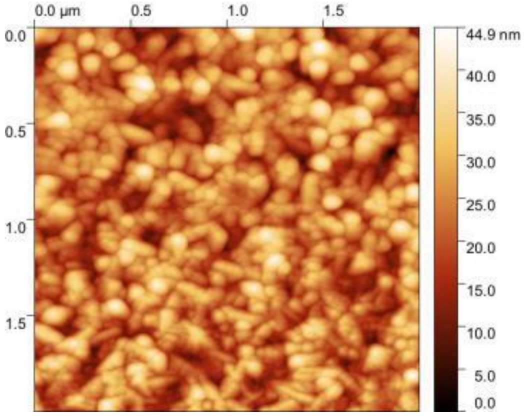

Figure 3-25. AFM topography image of the 1 µm thick pulsed DC reactive sputtered AlN film deposited with optimized conditions. RMS roughness was measured to be 3.94 nm.

3.4.6. SAW Device Performance

Figure 3-26 shows the photograph of a completed SAW device, an optical micrograph of the whole SAW chip, and magnified micrographs of part of the chip. Figure 3-27 shows the reflection coefficient of SAW devices fabricated with a 1 µm pulsed DC sputtered AlN film. The resonant frequency (f_r) of the SAW devices can be estimated by using the Equation (3.1), with surface acoustic wave velocity (v_{SAW}) being around 5050 ms^{-1}, and acoustic wavelength/ IDT electrode periodicity (λ) being 40 µm [13], [56].

$$f_r = v_{SAW}/\lambda \tag{3.1}$$

The estimated value of the resonant frequency obtained from the above equation is 126 MHz, but the reflection coefficient measurement, as shown in Figure 3-27, did not show any resonance peak. This is attributed to the insufficient quality of the AlN film layer in the SAW device.

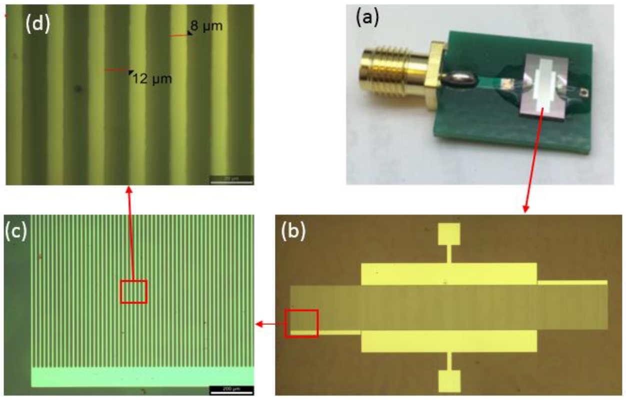

Figure 3-26. (a) SAW chip mounted on PCB and wire-bonded to PCB with SMA connector mounted on the edge of the PCB, (b) optical micrograph of the whole SAW chip, (c) and (d) optical micrograph part of the chip.

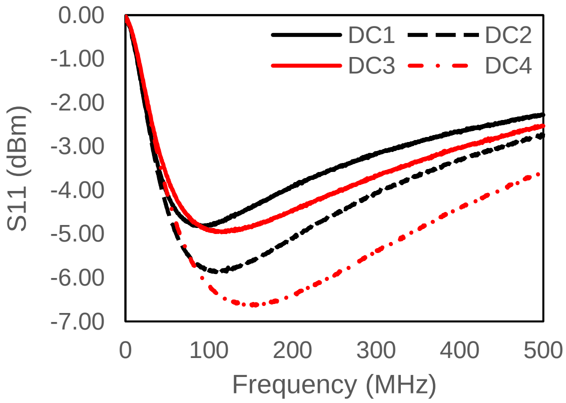

Figure 3-27. Reflection coefficients of surface acoustic wave devices with pulsed DC sputtered AlN. DC1 and DC2 have 200 interdigitated finger pairs, and DC3 and DC4 have 150 interdigitated finger pairs. DC1 and DC3 have a 1.42 mm aperture, and DC2 and DC4 have a 1.02 mm aperture.

3.5. Discussions and Conclusions

Polycrystalline [002] oriented aluminum nitride films were deposited using pulsed DC reactive sputtering. 50 % nitrogen was needed to deposit stoichiometric films with crystal growth in [002] orientation. With an increasing N_2 gas content, the intensity of the (002) peak increased but did not appear to influence the stoichiometry, morphology, or topography. Process pressure had the most significant influence on the film topography and morphology. For AlN films deposited at a process pressure of 1 mTorr, the RMS surface roughness (R_q) was found to be as low as 1.80 nm and Young's modulus reached a value of 312 GPa. These improved properties were due to the formation of a denser film at lower pressure.

Pulse frequency could influence the topographical and morphological of the AlN films. Increasing the frequency from 50 kHz to 200 kHz, the surface roughness (R_q) dropped to as low as 1.20 nm, and Young's modulus was increased to 335 GPa. The duty ratio did not appear to influence the film properties distinctively. A duty ratio of 0.8 at a frequency of 100 kHz is found to be optimum for growing AlN films with the highest Young's modulus and lowest surface roughness. AlN film of thickness 1 µm, deposited at 300 °C substrate temperature, 100% nitrogen as process gas, 1 mTorr process pressure, 100 kHz pulse frequency, and 80% pulse duty cycle resulted in best-optimized films with Young's modulus of 320 GPa and surface roughness of 3.94 nm, and best [002] orientation. However, the SAW device made from this AlN film did not show any resonance, which is attributed to the microstructure of the films. The SEM cross-sectional image revealed that the film grew with large crystallites and poor packing density.

CHAPTER 4: RADIOFREQUENCY SPUTTERING OF ALUMINUM NITRIDE THIN FILMS

4.1. Introduction

There has been a continued and increasing demand for piezoelectric materials for sensing and actuation in high temperatures and extreme weather applications such as automobiles, turbine engines, aircraft, nuclear reactor monitoring systems, and space applications [56]. Piezoelectric AlN films can operate at a very high temperature of around 1150 °C and possess a good piezoelectric coefficient of 5.5 pC/N [14]. AlN has the highest acoustic velocity of 5700 $ms^{-1,}$ among commonly used piezoelectric materials, whereas widely used quartz has an acoustic velocity of only 3200 ms^{-1} [37–39]. Hence, high-quality RF sputtered AlN is an attractive piezoelectric material for surface acoustic wave (SAW) devices for sensing at high temperature and high-frequency resonator applications. Fabrication of SAW devices requires (002) AlN film with the c-axis perpendicular to the surface and a very smooth surface [16,30,31,40].

In pulsed DC reactive sputtering, the hysteresis effect causes instability in the film growth process resulting from the target poisoning of the metal target in the presence of nitrogen gas [13]. The target voltage, associated with the pulsed DC sputtering, can be as high as 400 V. This high target voltage can sputter a few but extremely high-energy target particles, which can disrupt the film deposition on the substrate. Also arching on the target surface, caused by accumulated ions, can evaporate target droplets, which can cause non-uniformity of the deposited films [1,2]. RF sputtering can overcome these issues and can deposit high-quality films with smooth surfaces, and dense and fine crystallites with high packing density [1–3].

Considering the wide applications of AlN-based SAW devices, systematic exploration of influences of RF sputtering parameters, the insights of microstructure, and Young's modulus of piezoelectric AlN thin films are of vital interest. In this chapter, we present the deposition of [002] oriented piezoelectric AlN thin films from a ceramic AlN target. The process parameters such as temperature, pressure, and gas composition of the RF sputtering process were optimized by characterizing the surface roughness, X-ray diffraction, and Young's modulus of the deposited films. The optimized AlN films were utilized to fabricate SAW resonator devices with a film stack of Al/AlN/SiO_2 on a silicon wafer. Completed SAW devices were characterized by reflection coefficient (S_{11}) measurement to confirm the piezoelectric response of the AlN films. The performance of the surface acoustic devices was found to be influenced by piezoelectric film's thickness and device geometries, i.e., interdigital transducer fingers' number and aperture.

This chapter is written based on a manuscript under review titled, "*RF magnetron sputtering of piezoelectric AlN thin films for surface acoustic wave device*", by AA. Talukder, *et al*.

4.2. Previous Works

Sputtering deposition of AlN thin films from metallic Al target using pulsed DC reactive sputtering involves hysteresis effect which causes instability in the film growth process resulting from target poisoning in the presence of reactive nitrogen gas [13]. AlN film has been sputtered from a ceramic AlN target powered by an RF power supply with a more stable process by some researchers [7,36–38].

Numerous studies have been carried out on the fabrication of c-axis oriented AlN thin films deposited by DC reactive sputtering technique from Al targets [13,41–44,47,48,50]. For instance, Kar *et al.* reported their study on a reactive sputtering deposition of AlN thin films from a metallic Al target. They inspected the influence of deposition temperature and nitrogen gas content on electrical and morphological properties such as crystal orientation, bond formation, surface roughness, and grain size of the reactively sputtered AlN films. An increase in temperature was found to be associated with increased surface roughness and grain size. Higher nitrogen concentration resulted in smaller grain size and a smoother surface of the reactively sputtered film [45,46].

AlN film can also be prepared by using a ceramic AlN sputtering target powered by an RF power supply with a more stable process, but only a few relevant reports are available in the literature [16,57–59]. Singh et al. reported such studies on the fabrication of AlN thin films from ceramic AlN targets on various substrates, with varying RF power, process gas composition, and process pressure. They studied the effects of the substrate type and process parameters on the deposition rate, c-axis orientation, surface roughness, and film microstructure [16,58].

In another research, Bartsch *et al.* reported AlN films fabrication from a ceramic AlN target. They investigated the influence of substrate types and gas composition on the structural property, stress, and adhesion of the AlN film [60].

Though there have been numerous research studies on AlN film deposition from Al target using DC reactive sputtering, insufficient research on RF sputtering from ceramic AlN target-based deposition of piezoelectric AlN film has been reported. Also, most of the researchers reported studies on a single process parameter in each paper. Therefore, there is a lack of a comprehensive study on all these important parameters and requires an investigation of how the films' properties can be systematically optimized and applied to a SAW device. Also, there has been a need for studies on the influence of sputtering process parameters on the Young's modulus of AlN films. This chapter reports RF sputtering deposition of [002] oriented piezoelectric AlN thin films from a ceramic AlN target. The optimized AlN film was used to fabricate the SAW device to confirm the piezoelectric response of the AlN film.

4.3. Experimental Procedures

4.3.1. AlN Thin Film Deposition and Characterization

Silicon substrates (1” × 1”) were made by cleaving (100) silicon wafers. Silicon substrates were then cleaned ultrasonically in acetone and methanol in sequence for ten minutes in each solvent. Then the silicon substrates were blow-dried using a nitrogen gas-gun carefully. A sputtering deposition system (Kurt J. Lesker Company® PRO Line PVD 75) having three magnetrons sputtering sources (AlN, Al, and SiO_2 targets) and equipped with pulsed dc and radio frequency power supply, was used for the film deposition. Resistive-electric heaters were utilized to heat the substrate and maintain it at the desired temperature. The equipment automation of the system is accomplished via a standalone real-time controller. All the process parameters, i.e., substrate temperature, process gas flow rate, and rf power level, were controlled and monitored using the control software program. Table 4-1 shows the list of parameters of the RF sputtering process. Substrate temperature, process pressure, and nitrogen gas content were optimized step by step. The list of optimization parameters of the RF sputtering process is shown in Table 4-2.

The XRD measurements were carried out in a Rigaku SmartLab system with Cu-Kα radiation (λ-1.5406 Å). The surface topography and surface roughness (R_q) of the films were characterized using a *Hitachi AFM5100N* scanning probe microscope (SPM). The SPM was equipped with *μmasch’s HQ:NSC14/Al* tips (tip radius: 8 nm, tip height: 12-18 μm, tip cone angle: 40°, resonance frequency: 160 kHz, force constant: 5 N/m). The surface roughness (R_q) of the films was obtained from the SPM topographic image using *Gwyddion* SPM data analysis software. While evaluating surface roughness from the 2 μm × 2 μm SPM image, three evaluation scan lines each having lengths of 1.8 μm and a cutoff wavelength of 257 nm were used. A LAwave® (laser acoustic wave) system was used for determining Young's modulus of the AlN films [49]. Cross-sectional images of AlN film were taken using an ultra-high resolution JEOL 7500F field emission scanning electron microscope (FESEM).

Table 4-1. List of parameters of the RF sputtering process.

Target	3" AlN
Substrate	1" × 1" Si (100)
Substrate temperature	300 °C
Sputtering power	210 W (RF, 13.56 MHz)
Substrate temperature	20 – 500 °C
Process pressure	1– 5 mTorr
Process gas	Argon (Ar) and Nitrogen (N2)
Nitrogen gas content	10 – 50 %
Base pressure	2 x 10-7 Torr
Target to substrate distance	5.5 inches
Substrate rotation speed	10 revs/min
Temperature ramp up/down	10 °C/min
Magnetron ramp up/down	0.2 Watt/sec
Film thickness	200 ±10 nm

Table 4-2. List of optimization parameters of the RF sputtering process.

Study parameter	Temperature (°C)	Pressure (mTorr)	N2 gas content (%)
Temperature	varying: 20, 150, 300, 500	5	10
Pressure	300	varying: 1, 3, 5	10
N2 gas content	300	1	varying: 10, 25, 50

4.3.2. SAW Device Fabrication and Characterization

Silicon wafers with a diameter of 3” were used for making SAW devices. The wafers were cleaned with acetone and methanol, then blow-dried using a nitrogen gas gun. Then Kurt J. Lesker Company® PRO Line PVD 75 deposition system was used to sputter deposit SiO_2, AlN, and Al layers on the wafer. The deposition parameters of these layers are listed in Table 4-3. The top aluminum layer was patterned to obtain the IDT electrode using a photomask and aluminum etchant. A schematic diagram of the SAW device has been shown in Figure 3-2 in the previous chapter. Surface acoustic device chips were diced using an *ADT 7120* wafer dicing saw machine. Individual SAW chips were mounted on a printed circuit board (PCB), and wire bonded to an SMA connector mounted on the edge of the PCB. A network analyzer (300 kHz – 3 GHz, *Agilent Technologies*) was used to determine the scattering parameter, S_{11} of the devices.

Table 4-3. Sputtering process parameters of different layers of the SAW device.

Film (layer)	SiO_2 (bottom)	AlN (middle)	Al (top)
Pressure	5 mTorr	1 mTorr	4.5 mTorr
Temperature	200 °C	300 °C	25 °C
Power	200 W (rf, 13.56 MHz)	210 W (rf, 13.56 MHz)	100 W (pulse dc, 50 kHz, duty cycle: 75%)
Target	SiO_2	AlN	Al
Substrate	Si (100)	SiO_2/Si	AlN/SiO_2/Si
Process gas	Ar	50% Ar, 50% N_2	Ar
Thickness	500 nm	1 μm, 2 μm	150 nm

4.4. Results and Analysis

4.4.1. Effect of Substrate Temperature

Substrate temperature had a significant influence on the crystallinity and orientation of the deposited AlN films. Figure 4-1 shows the X-ray diffraction pattern of RF sputtered AlN thin films deposited at various substrate temperatures with 5 mTorr pressure and 10% N_2 concentration. The AlN crystals start to grow, preferably in the [002] direction at a substrate temperature of 150 ºC. At 300 ºC substrate temperature, the crystals almost only grew in the [002] direction indicated by a distinctive peak at 2θ of 36º. At a higher substrate temperature of 500 ºC, the crystals grow primarily in (101). So, a substrate temperature of 300 ºC was utilized in the following experiments.

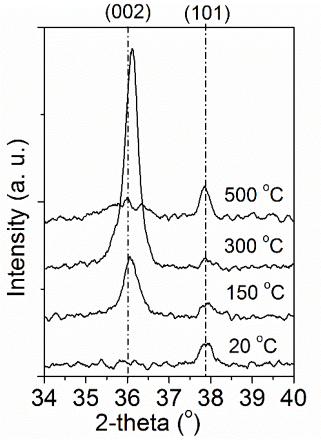

Figure 4-1. X-ray diffraction pattern of RF sputtered AlN thin films deposited at various substrate temperatures.

The substrate temperature was also affecting Young's modulus of the AlN films. Figure 4-2 shows Young's modulus of RF sputtered AlN thin films deposited at various substrate temperatures. Films deposited at a substrate temperature of 300 ºC had the maximum Young's modulus of 187 GPa, which is attributed to the highest crystallinity and maximum [002] orientation of crystallites, as shown in Figure 4-1. Films deposited at a higher or lower substrate temperature had weaker less/mixed oriented crystallinity hence resulting in lower Young's modulus.

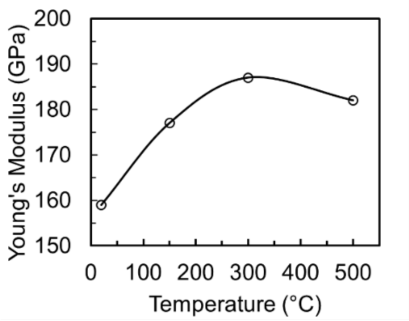

Figure 4-2. Young's modulus of RF sputtered AlN thin films deposited at various substrate temperatures.

4.4.2. Effect of Process Pressure

Process pressure has the most significant influence on the film's microstructure, topography, and morphology. Figure 4-3 shows the X-ray diffraction pattern of RF sputtered AlN thin films deposited at various process pressures, with 300 °C substrate temperature and 10% N_2 concentration. At lower process pressure, the film was more crystallized in [002] orientation, which is reflected in the XRD scan data presented in Figure 4-3. Any further reduction of process pressure was not feasible, as at pressure lower than 1 mTorr, plasma operation of the magnetron was not stable. At lower pressure, there are fewer collisions of the target material species with the background gas, resulting in higher energy of the depositing target material species. AlN species and molecules with higher energy could rearrange themselves to give rise to [002] orientation.

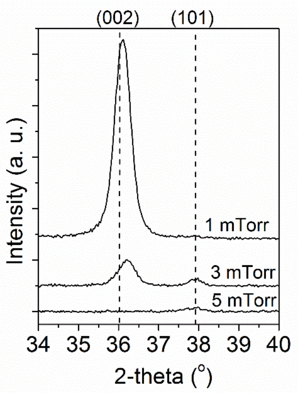

Figure 4-3. X-ray diffraction pattern of RF sputtered AlN thin films deposited at various process pressures.

Figure 4-4 shows the roughness and Young's modulus of AlN thin films deposited at various process pressures. Process pressure affected the surface roughness of the deposited AlN films significantly. With a decrease in the process pressure from 5 mTorr to 3 mTorr, surface roughness increased slightly, which can be attributed to the significant increase in crystallite size. Further increase in the process pressure to 1 mTorr reduced the roughness significantly to only 0.39 nm. This reduction in roughness can be attributed to the denser and smoother films resulting from depositing AlN particles with increased kinetic energies at this very low process pressure of 1 mTorr.

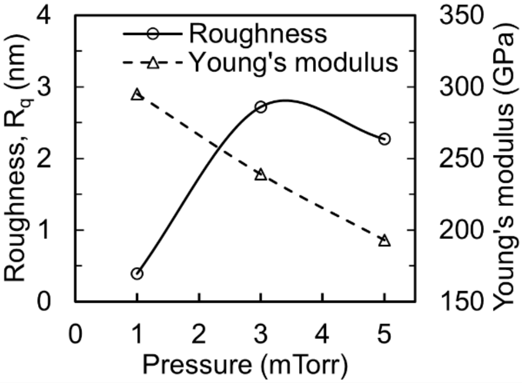

Figure 4-4. Roughness and Young's modulus of AlN thin films deposited at various process pressures.

Young's modulus is an indication of the density of the deposited AlN films. The Young's modulus of the films was influenced significantly by process pressure, as seen in Figure 4-4. With a decrease in the process from 5 mTorr to 1 mTorr, Young's modulus of the AlN film soared from 193 GPa to 295 GPa. As mentioned earlier, at lower process pressure, depositing AlN particles and molecules experienced fewer collisions with background process gases, hence processing higher kinetic energies. Deposition of AlN particles and molecules with higher kinetic energy resulted in more crystalline, dense, and high Young's modulus films.

A correlation between the film's Young's modulus and the ratio of (002) to (101) XRD peak was observed. As seen in Figure 4-3, there was a (101) peak in the film deposited at high pressure of 5 mTorr. With a decrease in process pressure, the intensity of that (101) peak decreased and vanished at a low process pressure of 1 mTorr. Moreover, with the reduction in process pressure, the intensity of that (002) peak increased. Figure 4-5 shows the correlation between Young's modulus and the XRD (002) to (101) peak ratio of AlN thin films. A higher value of (002) to (101) XRD peak ratio corresponds to a stronger preferred [002] orientation, hence higher Young's modulus of the film.

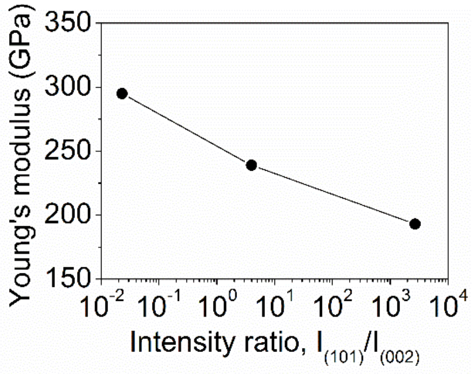

Figure 4-5. Correlation between Young's modulus and XRD (002) to (101) peak ratio of AlN thin films.

4.4.3. Effect of Process Gas Composition

RF sputtering of the AlN ceramic target normally leads to nonstoichiometric aluminum nitride films because of weaker nitride and stronger oxide formation [57]. An addition of a certain amount of nitrogen to the process gas is required to achieve a stochiometric AlN film and a preferred crystal growth in [002] orientation. Figure 4-6 shows the X-ray diffraction pattern of RF sputtered AlN thin films deposited with various nitrogen gas content in the Ar-N_2 process gas mixture. With the increase in N_2 content in the process gas mixture, [002] orientation of AlN increased, but it was found that 10 % N_2 was enough to achieve stoichiometric composition.

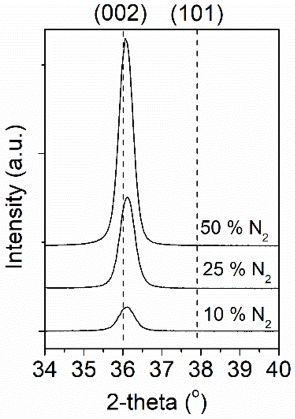

Figure 4-6. X-ray diffraction pattern of RF sputtered AlN thin films deposited with different nitrogen gas content in the Ar-N_2 process gas mixture.

Figure 4-7 shows the roughness and Young's modulus of RF sputtered AlN thin films deposited with different nitrogen gas content in the Ar-N_2 process gas mixture. The roughness of AlN films was almost similar and lower than 0.5 nm for all these films. Young's modulus of all the films was very close and just below 300 GPa. So, there is no real influence of the N_2 gas concentration on Young's modulus and roughness of the films with N_2 gas content above 10%.

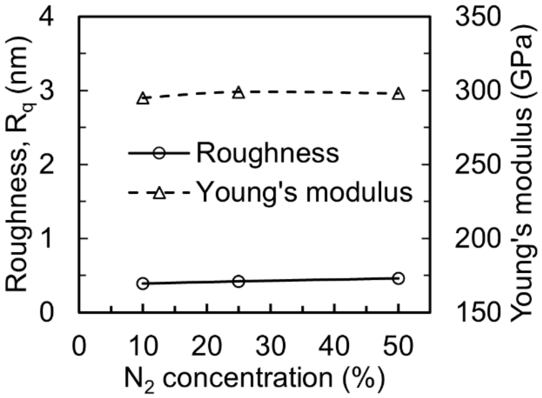

Figure 4-7. Roughness and Young's modulus of AlN thin films deposited with different nitrogen gas content in the Ar-N_2 process gas mixture.

4.4.4. Properties of 1 µm Thick AlN Film

Figure 4-8 shows the scanning electron microscope (SEM) image of a cross-section of a 1 µm thick AlN film grown on a silicon substrate. Columnar growth of AlN crystallites can be observed in the SEM image. Figure 4-9 shows the scanning probe microscope (SPM) topographic image of 1 um thick AlN film. The formation of small and dense crystallites of the RF sputtered films resulted in a very smooth surface having a surface roughness of only 0.71 nm, as seen in the SPM topographic image of Figure 4-9. Young's modulus of the film was found to be very high, ~325 GPa, which is attributed to the dense columnar growth of the film, as seen in the SEM image of Figure 4-8.

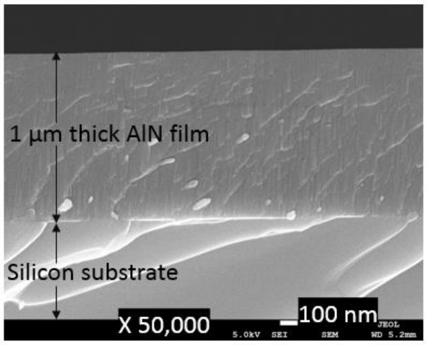

Figure 4-8. Scanning electron microscope image of a cross-section of the 1 um thick grown AlN film grown on a silicon substrate.

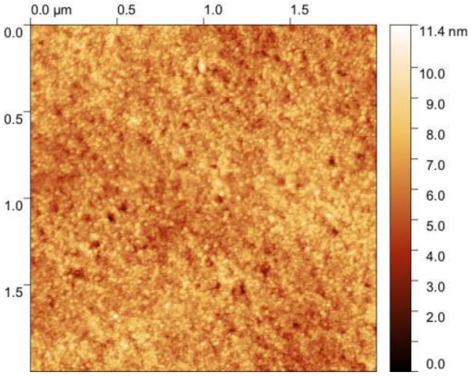

Figure 4-9. Scanning probe microscope topographic image of 1 um thick AlN film.

4.4.5. SAW Device Performance

Please refer to Figure 3-26 in Chapter 3 for the images of the fabricated SAW devices, with the only difference in the AlN layer which is visually similar. Figure 4-10 and Figure 4-11 show the reflection coefficient of SAW devices with AlN films having thicknesses of 1 µm and 2 µm, respectively. Table 4-4 summarizes the dimensions and performances of SAW devices. Devices with 2 µm thick and 1 µm thick AlN layers showed resonant frequency at ~125.6 MHz and ~126.8 MHz, respectively, which are almost the same. The sound velocity of surface acoustic waves (v_{SAW}) can be calculated from the resonant frequency (f_r) and the acoustic wavelength/ IDT electrode periodicity (λ), according to the equation (1) [13], [56].

$$v_{SAW} = f_r \times \lambda \tag{4.1}$$

Plugging the IDT electrode periodicity value of 40 µm into the equation (1), the sound velocity for the AlN films is calculated to be 5024 ms^{-1} and 5072 ms^{-1} for 2 µm and 1 µm AlN films, respectively. Similar sound velocity (~5050 ms^{-1}) of AlN was reported by Assouar et al. [32]. This slight difference, for 2 µm and 1 µm AlN films, is attributed to variation in the electrode/gap width of devices of two wafers. Reflection coefficient, S_{11} peak heights, and FWHMs were affected by the device geometry (aperture, number of fingers) and the AlN layer's thickness.

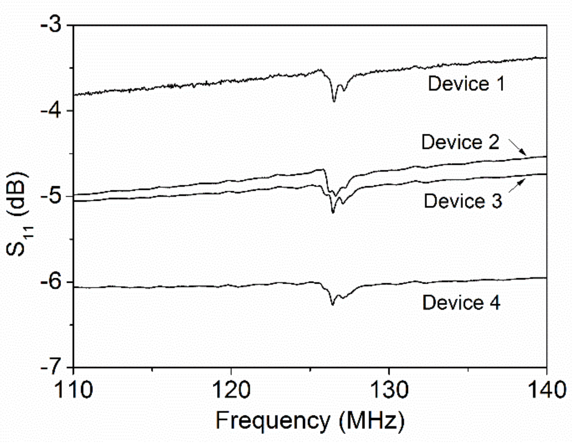

Figure 4-10. Reflection coefficients of SAW devices with 1 µm thick AlN film.

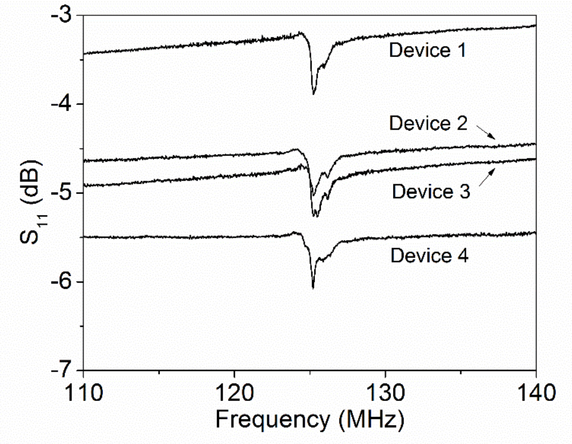

Figure 4-11. Reflection coefficients of SAW devices with 2 µm thick AlN film.

Table 4-4. Dimensions and performance parameters of SAW devices with 2 µm and 1 µm thick AlN film.

Device name	IDT electrode pair	Aperture (mm)	AlN layer thickness (µm)	Resonant frequency (MHz)	Q-factor
Device 1	200	1.42	2	125.6	133.3
			1	126.9	120.9
Device 2	200	1.02	2	125.7	103.4
			1	126.8	98.69
Device 3	150	1.42	2	125.6	83.7
			1	126.8	79.6
Device 4	150	1.02	2	125.6	77.6
			1	126.9	72.3

The performance of the surface acoustic devices was influenced by both the device geometry and the active piezoelectric AlN film thickness. Figure 4-12 shows the quality factors of the SAW devices with 1 and 2 µm thick AlN films. The quality factor of the device depends upon the interdigital transducer's geometry and the thickness of the underlying AlN film. The quality factor decreased with a reduction in aperture from 1.42 mm to 1.02 mm for device 1 and device 2, respectively, both having 200 finger pairs. The quality factor also decreased with a reduction in the number of finger pairs, from 200 to 150 for device 1 and device 3, respectively, both having the same aperture of 1.42 mm. A similar reduction in quality factor was observed for finger pair numbers of 200 and 150 for device 2 and device 4, respectively, both having the same aperture of 1.02 mm. Devices with 2 μm thick AlN films resulted in higher quality factors than devices with 1 μm thick AlN films, for any device geometry.

Doubling the AlN layer thickness increased the quality factor by 10.26 %, 4.77%, 5.15%, and 7.33% for device 1, device 2, device 3, and device 4, respectively. Comparing device 2 and device 1, a 39.2% increase (from 1.02 to 1.42 mm) in aperture, resulted in a 28.9% and 22.5% increase in quality factor for devices with 2 μm and 1 μm AlN films respectively. Contrasting device 3 and device 1, a 33.33% increase (from 150 to 200) in finger pair numbers, resulted in a 59.3% and 51.9% increase in quality factor, respectively, for 2 μm and 1 μm AlN films. While comparing device 4 and device 2, the quality factor increased by 33.2% and 36.5%, respectively, with 2 μm and 1 μm AlN films for a 33.33% increase (150 to 200) in the number of finger pairs.

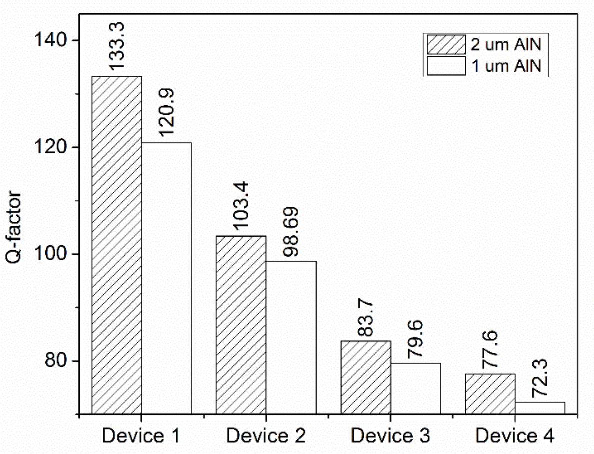

Figure 4-12. Quality factors of the SAW devices with 1 and 2 μm thick AlN film.

4.5. Discussions and Conclusions

Nanocrystalline aluminum nitride films, with c-axis orientation, were deposited from a ceramic AlN target by RF magnetron sputtering. AlN films, deposited at 300 °C substrate temperature, 50% nitrogen process gas, and 1 mTorr process pressure, resulted in films with the highest Young's modulus, and columnar growth. The piezoelectric property of the deposited AlN films was confirmed by a resonance peak at around 126 MHz in the reflection coefficient measurement of the surface acoustic device utilizing the optimized AlN film as an active layer. Sound velocity for the AlN films was calculated to be 5024 ms^{-1} and 5072 ms^{-1}, respectively, for 2 μm and 1 μm thick films. The thicker AlN layer resulted in a higher quality factor for the SAW devices, which was confirmed with four different electrode geometries of the SAW devices. The device with more interdigital transducer electrode pairs and wider aperture resulted in a higher amplitude of resonance peak and higher quality factor. The deposition parameters have strong effects on the AlN film structure, surface roughness, Young's modulus, and piezoelectric properties.

CHAPTER 5: ION SOURCE ENHANCED MAGNETRON SPUTTERING OF NITROGEN-DOPED ZING TELLURIDE THIN FILMS

5.1. Introduction

There has been an increasing interest in metal chalcogenide materials for their various optoelectronic applications in photovoltaics, light-emitting diodes, display devices, batteries, photocatalysis, etc. [62,63] These chalcogenide compounds include one or more chalcogen elements among sulfur, selenium, tellurium, and possesses semiconducting characteristics by bonding with transition metals. Among these chalcogenides, zinc telluride (ZnTe) is a direct and wide bandgap compound with a bandgap of 1.7–2.6 eV, which offers many applications [62–64].

ZnTe has a cubic diamond crystal structure, as shown in Figure 5-1, with a lattice constant of 0.6101 nm. ZnTe can also be grown in a hexagonal wurtzite structure. Undoped ZnTe offers p-type conductivity which is attributed to zinc vacancy defects in the lattice. ZnTe can be doped and used as semiconductor materials for optoelectronic applications including light-emitting diodes, laser diodes, and solar cells. ZnTe is used in solar cells as a back-surface field layer and p-type semiconductor material for a CdS/CdTe/ZnTe solar cell structure [64,65].

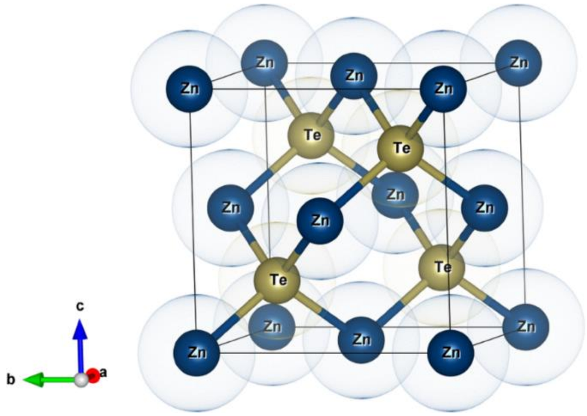

Figure 5-1. Cubic diamond crystal structure of zinc telluride [64].

For potential applications of ZnTe, it needs to be doped with a donor or acceptor to obtain a semiconducting ZnTe material. It is often desired to dope ZnTe with an acceptor dopant such as nitrogen, to enhance its intrinsic p-type conductivity [66,67]. There are research reports on the N-doping of ZnTe during the deposition process by introducing reactive nitrogen gas in the deposition chamber [67,68]. However, it is challenging to dope active N-atoms in the ZnTe compounds under common magnetron sputtering conditions. Also, there is a need for a method to modulate ZnTe:N film's microstructure by ion bombardment which is compatible with magnetron sputtering in a presence of the reactive nitrogen gas.

We studied ion source enhanced sputtering of N-doped ZnTe, which can deliver controlled ion energy and flux to achieve optimum ion-atom interactions. Conventional ion sources have limitations, such as being incompatible with reactive gases and unstable when operating with a magnetron [69,70]. Therefore, we develop and tested an innovative single beam ion/plasma source to enhance reactive magnetron sputtering and deposit ZnTe:N films, also with an ability to modulate the film's electrical and structural properties.

It is hypothesized that ion source enhanced magnetron sputtering can offer better control over the films' microstructure and N-doping than commercial magnetron sputtering. This proposed sputtering method utilizes a single beam ion source designed and patented by Q. Fan et al. [6]. This single beam ion source enhanced magnetron sputtering offers many advantages, such as decreased target voltage, sustaining the plasma at much lower pressure, providing additional energy to the depositing film, enhanced the deposition rate, and higher activation of the N-dopant.

Another hypothesis is that ion source enhanced magnetron sputtering could manage the inferior film quality of pulsed DC sputtering by eliminating the high energy particles described by

Thompson's distribution of energies of sputtered particles [71]. In Chapter 3 and Chapter 4 we presented the results of pulsed DC and RF sputtered AlN thin films, respectively.

Table 5-1 shows the comparison of the films and performances of the SAW devices. Both the films had preferred [002] orientation and similar Young's modulus. However, RF sputtered films had a smoother surface, and smaller & denser crystallites, which are desired attributes for thin film depositions. But RF sputtering process was much slower with about half the deposition rate of pulsed DC sputtering.

Table 5-1. Comparison of pulsed DC and RF sputtered films and SAW devices.

Deposition type	Deposition rate	Roughness (Rq)	Cross-sectional microstructure	SAW resonance peak
Pulsed DC	~ 4.5 nm/min	3.94 nm	columnar, larger crystallites with voids	No
RF	~ 2.2 nm/min	0.71 nm	columnar, smaller, and dense crystallites	Yes, at 125 MHz

According to Thompson's theory of atomic collision cascades, the kinetic energy E of a sputtered atom can be described by the probability density function [71],

$$F(E) = \begin{cases} A\dfrac{E[1-\sqrt{(E_b+E)/\Lambda E_i}]}{(E_b+E)^3} & if\ 0 \le E \le \Lambda E_i \\ 0 & if\ E > \Lambda E_i \end{cases} \tag{5.1}$$

with

$$\Lambda E_i = \frac{4m_i m_T}{(m_i + m_T)^2} E_i \tag{5.2}$$

ΛE_i is the maximum recoil energy, m_T and m_i are the molecular masses of the target and ion species, E_i is the incident ion energy, and A is a normalization coefficient. From Equation (5.2), maximum recoil energies for ion energies of 400 eV and 50 eV are 385 eV and 48 eV, using E_b=3.38 eV for Al target. An ion with 400 eV can sputter particles with energies up to 385 eV whereas the maximum sputtered particle energy can be only 48 eV for 50 eV sputtering ions. Thompson probability density function has been plotted in Figure 5-2, for two different ion energies of 400 eV and 50 eV.

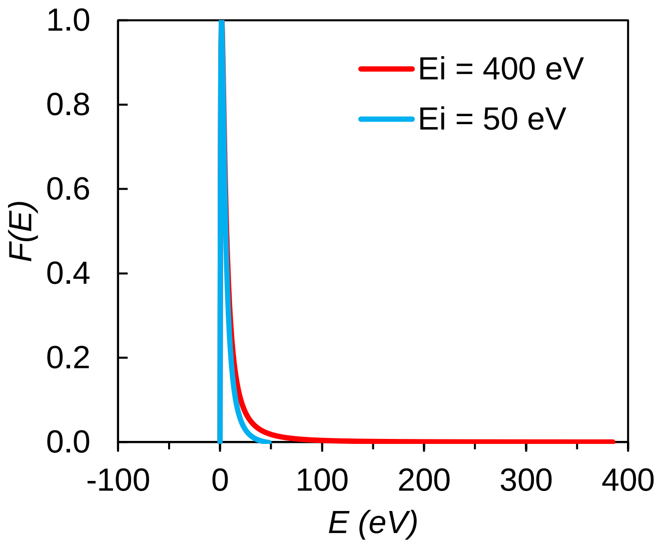

Figure 5-2. Thompson distribution of energies of sputtered particles.

Pulsed DC sputtering involved a high target voltage of above 400 V, as mentioned in Chapter 3. The sputtering ion energy (E_i) is proportional to the target voltage. The high target voltage could produce some extremely high energy particles, located in the tail of the Thompson probability density function, which might disrupt the nucleation process and deteriorated the film's quality. In the sputtering process, lowering the target voltage is expected to improve the film quality. One of the aspects of ion source enhanced magnetron sputtering is that it can lower the target voltage significantly, hence improving the quality of the deposited film.

The ion source enhanced magnetron sputtering uses a single beam ion source with a conventional magnetron. Figure 5-3 shows an illustration of thin film deposition by conventional magnetron sputtering and ion source enhanced magnetron sputtering. The average energy of the sputtered particles is around 10 eV for conventional magnetron sputtering, which is not enough to produce a dense film. Ion source enhanced deposition can overcome some of the limitations of pulsed DC magnetron sputtering. Ion source can lower the target voltage which will be presented in section 5.4.1, increase the nitrogen ionization and activation, and improve the ZnTe:N film quality as described below:

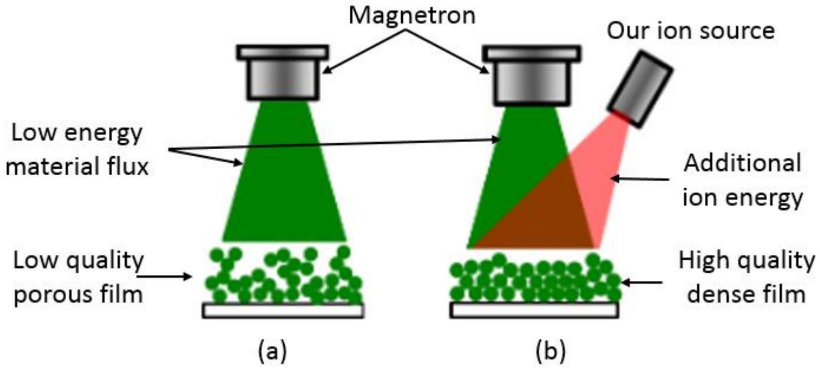

Figure 5-3. Thin film deposition by (a) conventional magnetron sputtering, and (b) ion source enhanced magnetron sputtering.

- Reduce in target voltage may truncate the high energy tail of the Thompson distribution of sputtered particle energy.
- Eliminating extremely high-energy particles from the tail can result in a better-quality film with nano-crystalline grains with an amorphous matrix.
- Increase ionization, and ions are driven toward the substrate by its positive potential and add energy to the growing film by ion bombardments.
- Increase activation and ionization of nitrogen, which helps in higher incorporation of active N-dopants to the film, hence efficient doping.

- Offer modulation of nitrogen doping, films resistivity, optical transmittance, and film's microstructural by adjusting ion source voltage.

Table 5-2 shows the state-of-the-art ZnTe:N sputtering deposition parameters and film properties. The industrial production line, utilizing pulsed DC sputtering, produces ZnTe:N films with a high resistivity of 71.5 Ω-cm, deposited at 230-265 °C substrate temperature. The solar cell production requires ZnTe:N films with a resistivity of about 10 Ω-cm and peak optical transmittance of >60%. RF sputtering process can result in resistivity of the film as low as 5.0 Ω-cm. But the RF sputtering is not suitable for the production line for its low deposition rate. Also, the ZnTe:N films need to be deposited at a substrate temperature of <200 °C to maintain the process compatibility of the solar cell production line. Our research will consider these constraints and demonstrate the ion source enhanced growth of the ZnTe:N films with a resistivity of ~10 Ω-cm using the pulsed DC sputtering process and process temperature of 200 °C.

Table 5-2. State-of-the-art ZnTe:N sputtering deposition parameters and film properties.

Deposition type	RF sputtering (lab data)	Pulsed DC sputtering (production data*)
N_2 flow (%)	1.5	6
Pressure (mTorr)	6	6
[N] in film (cm^{-3}) (DSIMS)	5×10^{20}	3.5×10^{20}
Hall carrier density, N_a (cm^{-3})	2×10^{18}	4.6×10^{17}
Activation (%)	0.40	0.15
Hall mobility, μ (cm^2/V-s)	0.64	0.19
Resistivity (Ω-cm)	5.0	71.5

* data colledted through internal communication.

This chapter is written based on a manuscript under review titled, “*Efficient nitrogen doping of zinc telluride thin film by ion source enhanced magnetron sputtering,”* by AA. Talukder, *et al*.

5.2. Previous Works

Nitrogen-doped ZnTe has been widely studied for its application as a buffer layer for back contact of CdS/CdTe solar cells. To increase the efficiency of CdTe solar cells beyond 16%, a back contact with ideally zero valence-band offset and high conduction-band offset with CdTe is required for easy flow of majority carriers to the metal back contact [67,72–74]. Typically, ohmic contacts are prepared for CdTe by diffusing copper to form a thin space charge layer, which can easily be tunneled. Copper is a fast migrating impurity in CdTe and can degrade the solar cell performance [75,76]. To overcome this problem to ZnTe:N film has been utilized as a buffer layer with a high work function between the CdTe surface and metal contact [67,72].

ZnTe films have been deposited using various vapor phase or solution-based techniques including molecular beam epitaxy, evaporation, pulsed laser deposition, reactive sputtering, and electrodeposition [64,67,72,77–80]. The molecular beam epitaxy process has been reported to produce a high-quality film with a high level of carrier density [26,77,79]. However, high equipment cost and low deposition rate (~ 1 monolayer/ second) make molecular beam epitaxy unappealing for economic and large volume production. Magnetron sputtering, a low-cost and convenient process, has been found to produce ZnTe:N films with reasonable and comparable carrier density. Nitrogen doping level has been controlled by adjusting the reactive nitrogen gas flow during the sputtering process [66,67].

Späth et al. reported their research on the N-doping of ZnTe and its influence on the CdTe/ZnTe interface [67]. They fabricated the p-type ZnTe:N film by thermal evaporation of the compound and an additional nitrogen plasma source was used to control the p-doping of the ZnTe film. The resistivity was measured by four-point measurements and a minimum resistivity of 0.04 Ω-cm was reported. This group deposited the ZnTe:N film with a source temperature of T=680 °C and substrate temperature of 350 – 425 °C. The plasma source was operated at a vacuum pressure of $P_{N2} = 10^{-5}$ mbar.

Nitrogen doping during pulsed laser deposition (PLD) of p-type ZnTe thin films was reported by Su Lee et al [80] For the PLD process, they used the ZnTe target and deposited the ZnTe:N film on a sapphire substrate maintained at 250 ºC. The partial pressure of nitrogen was varied from 0.1 – 70 mTorr. They obtained low resistivity at higher nitrogen partial pressure; 54.9 and 9.32 Ω-cm for 50 and 70 mTorr nitrogen partial pressure. They also reported that with an increase in the nitrogen partial pressure the crystallinity (cubic zinc-blende) of the ZnTe film was degraded significantly.

Rakhshani et al. reported their work on nitrogen doping of ZnTe thin film for fabricating ZnTe/ZnO light-emitting diode [68]. They fabricated the p-type ZnTe thin film by magnetron sputtering from a ZnTe target in a nitrogen/argon gas mixture and the borosilicate glass substrate was kept at 300 ºC. This research varied the nitrogen flow rate from 0 to 10% and studied the influence on ZnTe:N films crystal size, transmittance, bandgap, resistivity, carrier concentration, and hall mobility. They reported the highest hole density of 2.5×10^{18} cm^{-3} and lowest resistivity of 1.5 – 2.7 Ω-cm for a nitrogen flow rate of 2-4%.

In another study, Shimpi et al. reported N-doping of ZnTe thin films fabricated from ZnTe target by RF magnetron sputtering and introducing N_2 gas to the chamber [65]. They used a glass substrate and substrate temperature of 350 ºC. Nitrogen gas flow was varied from 0% to 5%, and the ZnTe:N films were characterized for crystallinity, optical transmittance, bandgap, and electrical properties. With an increase in the nitrogen flow, there were decreases in optical transmittance, bandgap, ZnTe (111) intensity, and an increase in (111) peak broadening. They reported the lowest resistivity of 31 Ω-cm for 0.5 % nitrogen gas flow and highest carrier concentration of 6.85×10^{17} cm^{-3} for 0.85 % nitrogen gas flow, and highest mobility of 0.636 $cm^2/(V.s)$ for the lowest nitrogen flow of 0.35%.

As found from the literature, nitrogen doping of ZnTe films has been done either by introducing nitrogen gas in a sputtering process or by utilizing a nitrogen ion source in ZnTe evaporative deposition method [67,68,72,81]. There has been a lack of research on the utilization of ion sources in magnetron sputtering for the controlled N-doping of ZnTe films. Most of the reported works utilized ion source/ ion beam, which requires filament to produce the ions, are unsuitable for the sputtering method which involves reactive gas and operates at a different pressure than the ion beam operating region [69,70]. Our research fills this gap of research and demonstrates the advantages of the novel ion source enhanced magnetron sputtering over conventional magnetron sputtering through the modulation of electrical, optical, and structural properties of the deposited ZnTe:N films.

5.3. Experimental Procedures

A sphere-shaped vacuum chamber was used for the ion source enhanced deposition process. Figure 5-4 shows a schematic of the ion source enhanced magnetron sputtering system. The magnetron and the ion source were installed from the top and side flanges of the chamber, respectively. A substrate shutter (not shown in the schematic) was also installed from the tap flange to facilitate pre-sputtering of the target before each deposition to clean up any contamination on the target and to achieve stabilized and consistent plasma discharge during each deposition. The substrate stage had arrangements of heating and rotation.

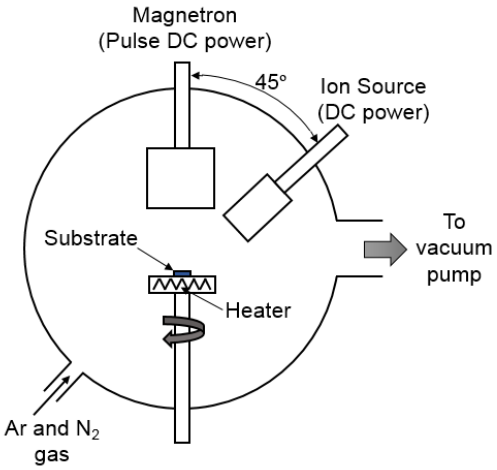

Figure 5-4. Schematic of the ion source enhanced magnetron sputtering system.

Soda-lime glass substrates were cleaned in an ultrasonic bath in acetone and isopropanol, for 10 minutes in each solvent. The cleaned substrates were dried using a nitrogen gas blow-gun. The cleaned and dried substrates were loaded to the chamber using the load lock system. Table 5-3 lists all the parameters of the ion source enhanced magnetron sputtering process. A preheating of the substates was done inside the chamber for uniform heating over the substrate. A 3-inches ZnTe target was mounted on the magnetron and the magnetron was powered by pulsed DC power with constant power mode. The ion source was powered by DC power with constant voltage, within the range of 0 V - 140 V. Magnetron power was adjusted between 40 W - 25 W when the ion source was used, to maintain a similar deposition rate. After deposition, a cool downtime of 40 minutes was maintained before taking the deposited substrate out of the chamber to eliminate any thermal shock to the film. 100 nm thick films were deposited for all studies. Only for ion source voltage studies, 17 nm films were also deposited, besides 100 nm films. The resistivity of the films was characterized by using six-point probe measurements. X-ray photoelectron spectroscopy and X-ray fluorescence measurements were used for the quantitative elemental composition characterizations. XRD measurements of the films were carried out by using a Rigaku SmartLab system with Cu-Kα radiation (λ= 1.5406 Å).

Table 5-3. Parameters of the ion source enhanced magnetron sputtering of the ZnTe:N films.

Target	Ø 3” Zinc telluride
Substrate	Soda-lime glass (1.5” × 1.5”)
Substrate temperature	200 °C
Substrate preheating/ after-cooling	40 min
Magnetron power	25-40 W (pulsed DC with f = 100 kHz, Trev = 1 μs)
Ion source voltage	0 – 140 V
Deposition time	40 – 45 sec (17 nm film); 3.5 – 4 min (100 nm films)
Film thickness	17nm and 100 nm
Process gas	Argon (Ar) and Nitrogen (N2)
Base pressure	5 x 10-7 Torr
Process pressure	3 – 8 mTorr
Substrate – target/ ion source distance	4.5 inch
Substrate rotation speed	10 revs/min

5.4. Results and Analysis

5.4.1. Plasma Discharges of Ion Source Enhanced Magnetron Sputtering

Figure 5-5 shows plasma discharges of ion source enhanced magnetron sputtering with different ion source voltages. The ion source voltages were 0 V, 80 V, 120 V, and 140 V, from left to right. All the discharges were done at a pressure of 6 mTorr and process gas of 5% N_2 and 95% Ar. Target powers were 40W, 32 W, 25 W, and 25W ion source voltage of 0 V, 80 V, 120 V, and 140 V, respectively. Target power was reduced with an increase in the ion source voltage to maintain a similar deposition rate. With the increase in ion source voltage, the plasma color turned from red-orange to more pink, indicating higher activation of nitrogen in the plasma. Target voltages were reduced from 238 V for 0 V ion source voltage to 210 V, 171 V, and 159 V for the ion source voltages of 80 V, 120 V, and 140 V, respectively.

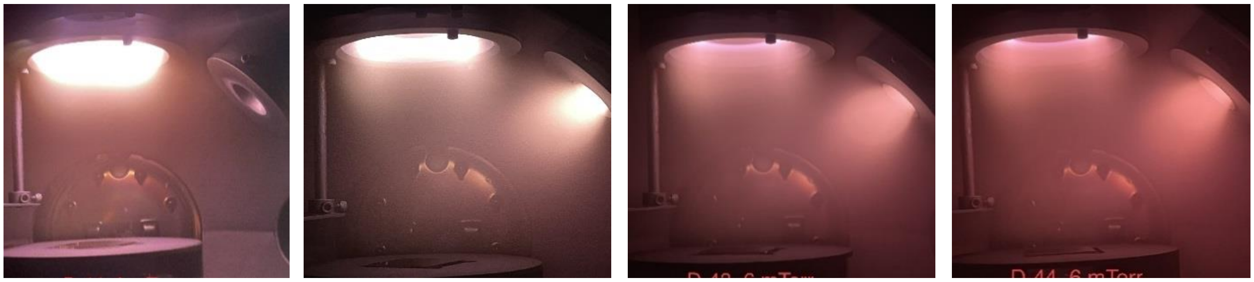
(a) (b) (c) (d)

Figure 5-5. Plasma discharges of ion source assisted magnetron sputtering with different ion source voltages, magnetron power, and magnetron voltages of (a) 0V, 40 W, 238 V (b) 80 V, 32 W, 210 V (c) 120 V, 25 W, 171 V and (d) 140 V, 25 W, 159 V, respectively.

5.4.2. Effect of Nitrogen Concentration

Figure 5-6 shows the resistivity, Zn/Te atomic ratio, and N density of ZnTe:N films deposited with various N_2 gas flows. Without the ion source, the resistivity of the ZnTe:N film was very high if the N_2 gas flow rate was below 5%, as seen in Figure 5-6 (a). The N_2 flow rate needs to be above 5% to get low resistivity without the ion source. Ion source enhanced deposition could lower the resistivity to <30 Ω-cm with only a 2% - 5% N_2 flow rate. The ion source enhanced nitrogen doping efficiently even at a low nitrogen flow. However, at a higher nitrogen flow rate above 5%, the resistivity went to a higher value. This is attributed to the too much uptake of nitrogen dopant, hence deteriorated structure and decreased carrier mobility in the film.

Figure 5-6 (b) shows the Zn/Te atomic ratio of ZnTe:N films deposited with various N_2 gas flow with and without an ion source. Without the ion source, with an increase in the nitrogen flow, the Zn/Te atomic ratio increased. With the increase in N_2 flow, more and more N dopants replaced the Te lattice site and causing the Zn/Te ratio to go higher. An ion source could enhance this phenomenon of N replacing Te and result in a higher Zn/Te ratio than without an ion source, up to

~6% N_2 flow. Beyond 5% N_2 flow with the ion source, the Zn/Te ratio started to drop, which can be attributed to the uptake of the interstitial N rather than replacing the Te lattice sites. Figure 5-6 (c) shows the N density of ZnTe:N films deposited with various N_2 gas flow with and without the ion source. With an increase in the N_2 flow, for both cases, N uptake kept increasing. The ion source could result in higher N uptake in the film in any N_2 flow.

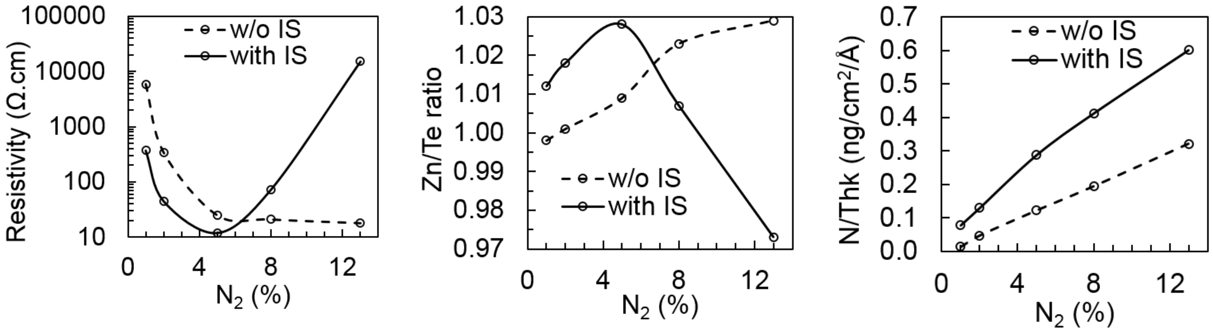

(a) (b) (c)

Figure 5-6. (a) Resistivity, (b) Zn/Te atomic ratio, and (c) N density of ZnTe:N films deposited with various N_2 gas flows.

Figure 5-7 shows the influence of nitrogen flow on the transmittance of the ZnTe:N films deposited by magnetron sputtering. With an increase in the N_2 flow, the transmittance of the film continued to drop which is undesirable for optoelectronic applications of the film. With too much N_2 flow the N uptake to the film is too high and the structure of the film might get worse and resulted in low transmittance. As discussed earlier in this section, to have low resistivity of the film the deposition needs to be done with high N_2 flow (>5 %) without an ion source, as seen in Figure 5-6 (a). But with high N_2 flow of above 5% caused the transmittance of the film to drop significantly, as seen in Figure 5-7.

Figure 5-8 shows the impact of ion source on the transmittance of ZnTe:N films with low (1 – 5 %) N_2 flow and high (8 – 12 %) N_2 flow. If the N_2 flow is relatively low (1 – 2 %), the ion source could increase the transmittance significantly, as seen in Figure 5-8 (a). As N_2 flow approached 5 %, the ion source just started to decrease the transmittance. However, as the N_2 flow is increased to 8 – 13% the ion source decreased the transmittance of the ZnTe:N film, as seen in Figure 5-8 (b).

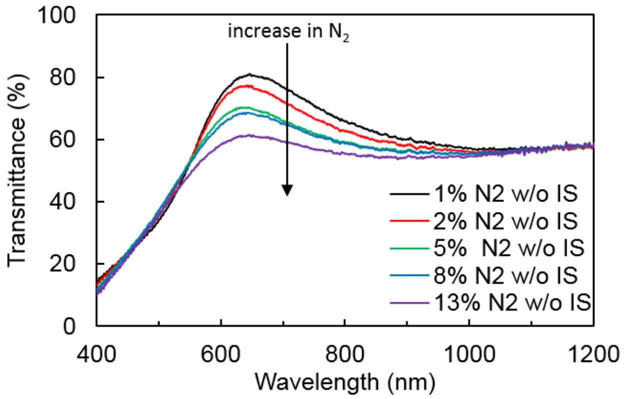

Figure 5-7. Influence of nitrogen flow on the transmittance of the ZnTe:N films deposited by magnetron sputtering.

In summary, to get low resistivity (<30 Ohm-cm) with conventional magnetron sputtering, N_2 flow needs to be quite high (8 – 12 %), which sacrifices the transmittance of the film significantly. Ion source enhanced magnetron sputtering requires only 2 – 5 % N_2 flow for achieving both low resistivity and higher transmittance than conventional magnetron sputtering.

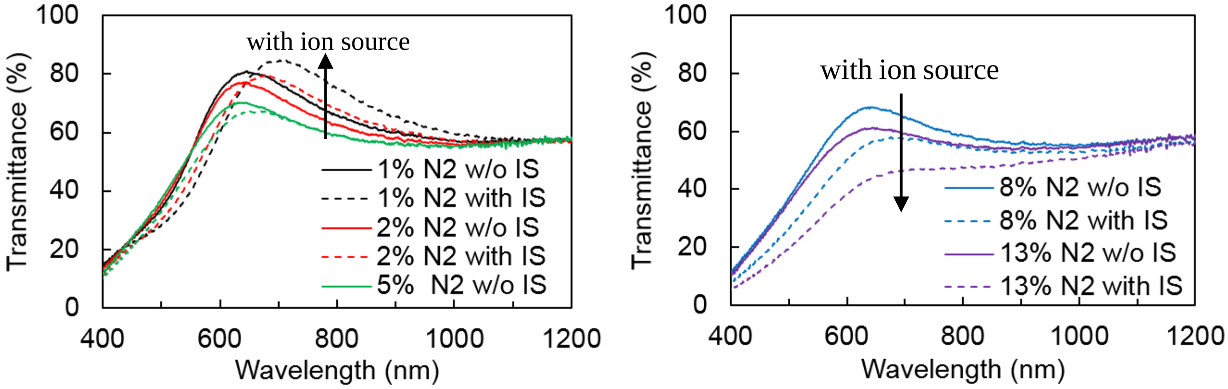

(a) (b)

Figure 5-8. Impact of ion source on the transmittance of ZnTe:N films with (a) low (1 – 5 %) N_2 flow and (b) high (8 – 12 %) N_2 flow.

5.4.3. Effect of Ion Source Voltage

Figure 5-9 shows the resistivity, Zn/Te atomic ratio, and N density of ZnTe:N films with a thickness of 17 nm and 100 nm, deposited with various ion source voltages. 100 nm films had lower resistivity than 17 nm films by almost 10 times, at any ion source voltage, as seen in Figure 5-9 (a). At the lower thickness of 17 nm, besides the surface scattering effect, the film could not have as good structural properties and N-doping as 100 nm film. For both films, the resistivity was lowest with ion source voltage between 80 – 120 V. However, 120 V ion source voltage was used in subsequent experiments to ensure enough impacts from the ion source in the deposition process.

Figure 5-9 (b) and (c) show the Zn/Te atomic ratio and N density of ZnTe:N films with a thickness of 17 nm and 100 nm, deposited with various ion source voltages. 100 nm films had a higher Zn/Te ratio and N-density at any ion source voltage. Thicker films took a long time and could uptake more N dopants in the film, resulting in a higher Zn/Te ratio and N density. Also, with an increase in the ion source voltage, both Zn/Te ratio and N density increased. This is attributed to the fact that at higher IS voltage, there were more activation and ionization of N atoms, hence more uptake of N atoms to the depositing film.

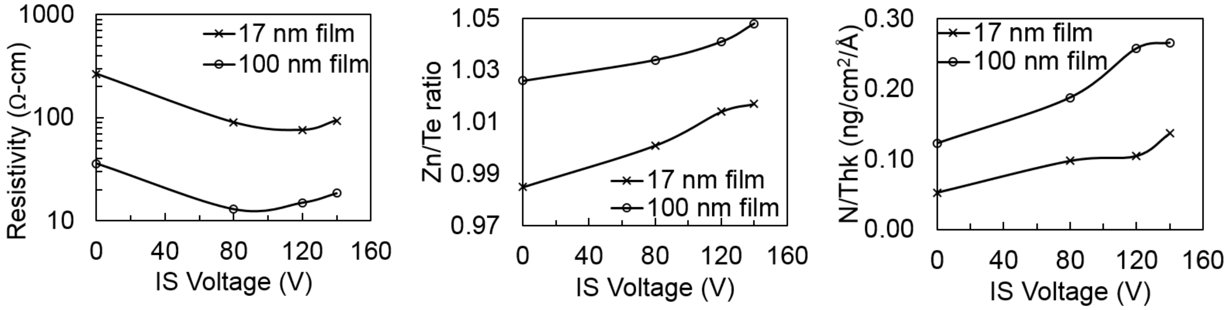

(a) (b) (c)

Figure 5-9. (a) Resistivity, (b) Zn/Te atomic ratio, and (c) N density of ZnTe:N films deposited with various ion source voltage.

Figure 5-10 shows the XRD patterns of ZnTe:N thin films deposited with (IS voltage: 120V) and without the ion source. The XRD peak for the cubic (111) plane is reported to be at 2θ = 25.26° for powder ZnTe (Ref code 15-746). Both the films showed three peaks at ~25.4º, ~ 42º, and 49.7º which corresponds to (111), (220), and (311) planes of cubic ZnTe lattice, respectively. Considering the (111) plane, ZnTe:N film deposited with ion source (ion source voltage: 120V) had a smaller peak with wider FWHM than the films deposited without ion source (ion source voltage: 0V). This indicates that the film deposited with the ion source has smaller crystallites.

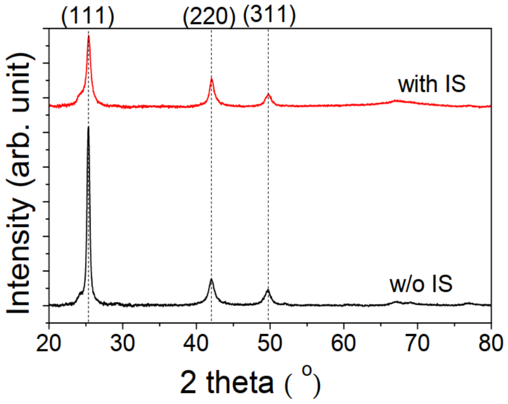

Figure 5-10. XRD patterns of ZnTe:N thin films deposited with (IS voltage: 120V) and without ion source.

Figure 5-11 and Figure 5-12 show the TEM images of ZnTe:N films deposited without the ion source and with the ion source at a lower and higher level of magnification, respectively. TEM images in Figure 5-11 show, that films deposited without the ion source had larger crystals than the film deposited with the ion source, which is analogous to the XRD results. At a higher magnification TEM image, as shown in Figure 5-11, it may appear difficult to confirm the difference between the microstructures of the film deposited without and with the ion source.

However, at lower magnification, as shown in Figure 5-12, the difference in the microstructure is obvious. TEM image of the film deposited without the ion source shows more and larger crystallites than the film deposited with the ion source enhancement, as seen in Figure 5.12 (a) and Figure 5.12 (b), respectively.

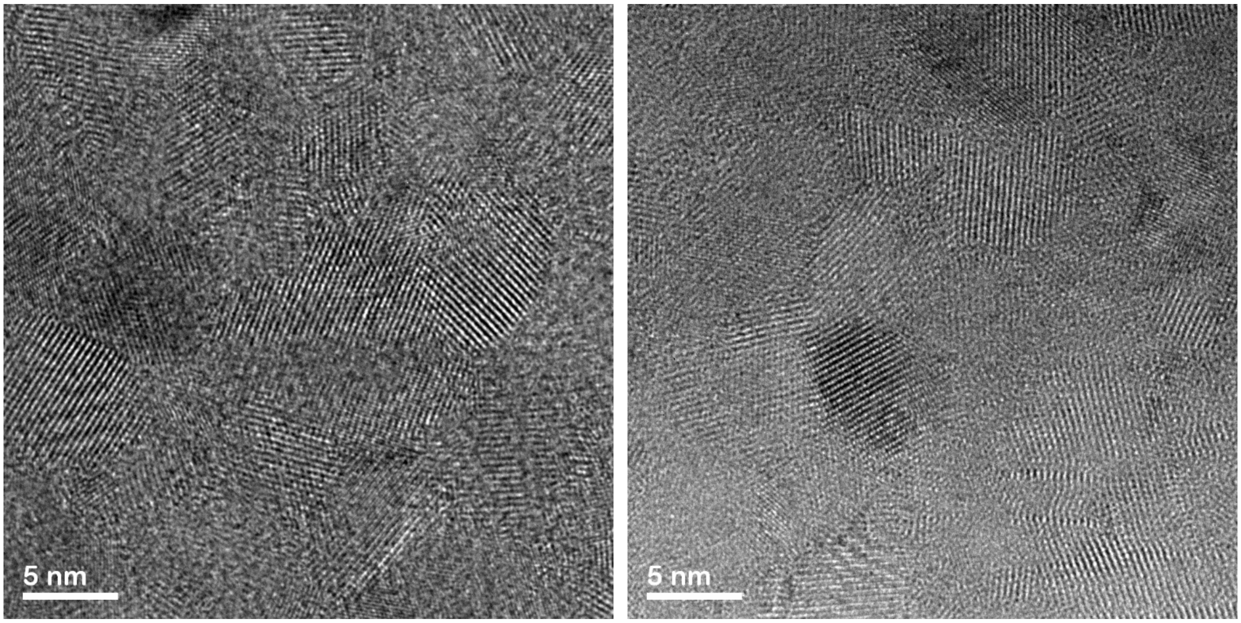

(a) (b)

Figure 5-11. TEM images of 17 nm ZnTe:N film deposited (a) without IS and (b) with IS.

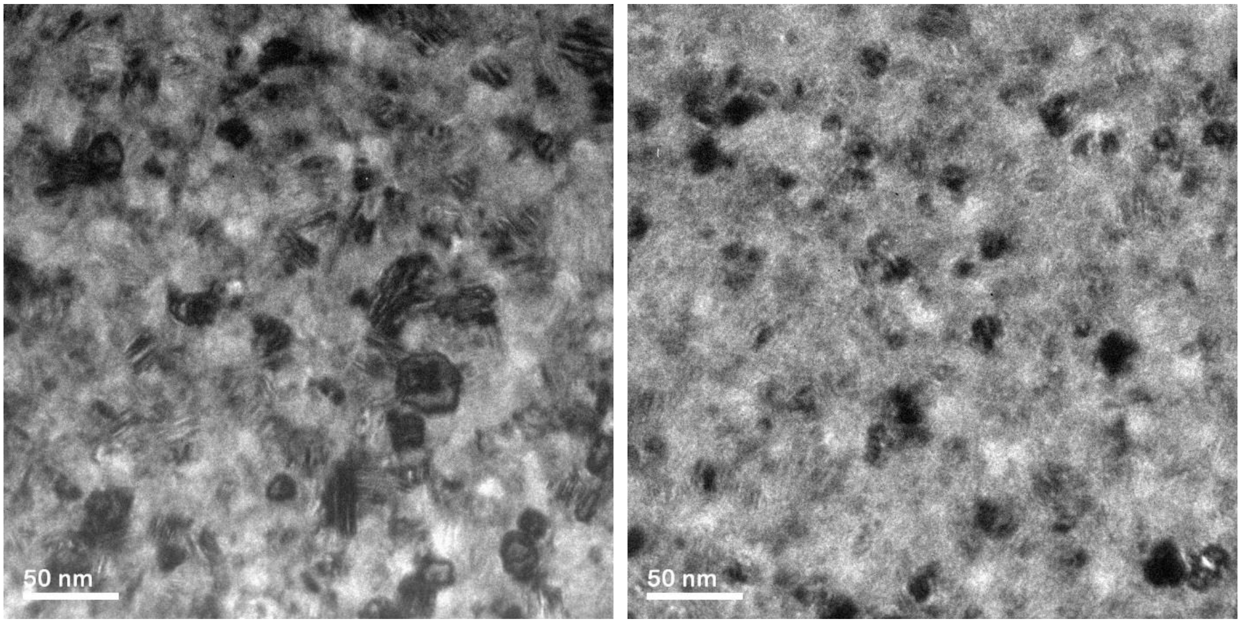

(a) (b)

Figure 5-12. TEM images of 100 nm ZnTe:N film deposited (a) without IS and (b) with IS.

Figure 5-13 shows the (111) peak position, (111) d-spacing, and (111) FWHM of ZnTe:N films deposited with various ion source voltages. With an increase in ion source voltage, the (111) peak shifted toward higher 2-theta values, maxed out at 120 V, and then shifted to lower 2-theta at 140 V, as seen in Figure 5-13 (a). The d-spacing has been calculated using the equation (5.3), where λ (=1.5406 Å) is the X-ray wavelength, n (=1) is the order of refraction, and θ is obtained from the 2θ position of the (111) peak. Figure 5-13 (b) shows the d spacings of (111) plane of ZnTe:N films deposited with various ion source voltages.

$$d = \frac{n\lambda}{2\sin\theta} \tag{5.3}$$

As the d spacing is inversely proportional to the position of the (111) peak, the d spacing curve follows an opposite trend to that of the (111) peak position curve, as seen in Figure 5-13 (b). The d spacing of the (111) plane hits a minimum value at an ion source voltage of 120V, meaning the densest crystallites for this case. This shrinking in d spacing can also be attributed to the formation of dense amorphous film around the crystallites, which compressed the crystals and caused smaller d spacing. The FWHM of the (111) peak increased with an increase in the ion source voltage, maxing out at 120 V and then dropping back to a lower value at 140 V, as seen in Figure 5-13 (c). This indicates the ion source could make finer crystallites and the effect was maximum at 120 V.

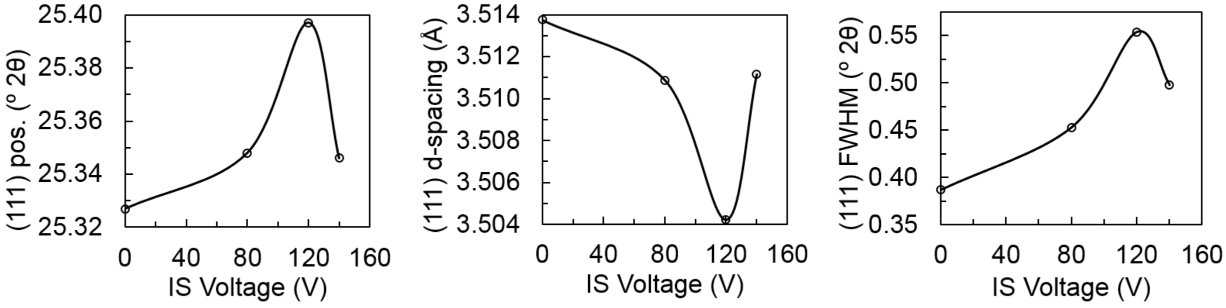

(a) (b) (c)

Figure 5-13. (a) (111) peak position, (b) (111) d-spacing, and (c) (111) FWHM of ZnTe:N films deposited with various ion source voltages.

5.4.4. Effect of Process Pressure

Figure 5-14 shows the impacts of ion source on the resistivity, Zn/Te ratio, and N uptake in the ZnTe:N films, deposited at three different pressure levels. Figure 5-14 (a) shows the resistivity of the ZnTe:N films deposited with and without ion source deposited at 3, 6, and 8 mTorr. Ion source enhanced deposition decreased the resistivity of the film deposited at 3 mTorr and 6 mTorr pressure. The decrease in the resistivity is attributed to the increased N-doping and higher activation of the N-dopants in the film. The decrease in the resistivity is also attributed to the improved structural property of the film, contributed by the additional energy provided by the ion source. However, the resistivity of the film, deposited at higher pressure i.e., 8 mTorr, increased by the ion source. At higher pressure of 8 mTorr with the ion source, the level of N dopants uptake to the film is higher than the optimum level, mimicking the scenario of higher nitrogen gas, resulting in lower resistivity.

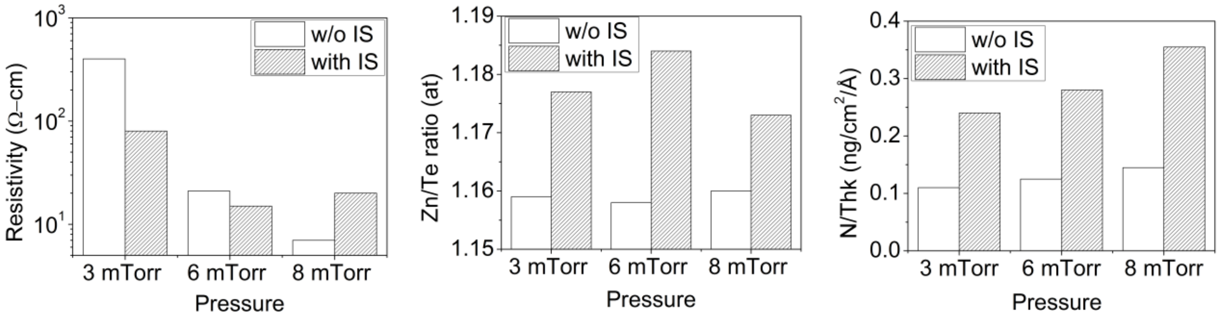

(a) (b) (c)

Figure 5-14. (a) Resistivity, (b) Zn/Te atomic ratio, and (c) N density of ZnTe:N films deposited with and without ion source at various process pressures.

Figure 5-14 (b) shows the Zn/Te atomic ratio of the films deposited with and without an ion source at three different pressure levels, i.e., 3 mTorr, 6 mTorr, and 8 mTorr. For any process pressures, ion source enhanced deposited films had a higher *Zn/T*e ratio, meaning higher *Te* vacancies in the film. These *Te* vacancies were occupied by the *N*-dopants which contributed to the conductivity of the ZnTe film.

Figure 5-14 (c) shows the nitrogen density of the films deposited with and without the ion source at various pressures. For all three process pressures, ion source enhanced deposition could increase the nitrogen uptake in the film. The ion source could create more nitrogen ions and free radicals in the plasma which could increase the incorporation of nitrogen atoms in the growing films. Following calculations can roughly estimate the nitrogen doping level from the nitrogen density, presented in Table 5-4. Ion source enhanced deposition enhanced the N-doping level for all three process pressures.

$$Nitrogen\ density\ (g.cm^{-3}) = \frac{x \times 10^{-9} g}{1\ cm^2\ \times 10^{-8}\ cm} = 0.1x\ g.cm^{-3}$$

$$where\ x\ [ng/cm^2/\text{Å}]\ is\ the\ N\ density\ in\ the\ film$$

$$Nitrogen\ atomic\ density\ (atoms.cm^{-3}) = \frac{Nitrogen\ density\ (g.cm^{-3})}{Mass\ of each\ N\ atom\ (g.atom^{-1})}$$

$$= \frac{0.1x\ g.cm^{-3}}{14.0067\ \times 1.67377 \times\ 10^{-24}\ (g.atom^{-1})} = 4.27x\ \times\ 10^{21}\ atoms.cm^{-3}$$

$$ZnTe\ molecular\ density\ (molecules.cm^{-3})\ in\ perfect\ stoichimetry$$

$$= \frac{ZnTe\ density\ (g.cm^{-3})}{Mass\ of each\ ZnTe\ molecule\ (g.atom^{-1})}$$

$$= \frac{6.34\ g.cm^{-3}}{(65.38 + 127.6)\ \times 1.67377 \times\ 10^{-24}\ (g.molecule^{-1})}$$

$$= 1.96 \times\ 10^{22}\ molecules.cm^{-3}$$

$$Doping\ level\ \left(\frac{N\ atom}{ZnTe\ molecule}\right) = \frac{4.27\ \times\ 10^{21}\ atoms.cm^{-3}}{1.96 \times\ 10^{22}\ molecules.cm^{-3}}$$

$$= 0.2176x = 21.76x\ \%$$

Table 5-4. The calculated nitrogen doping level of the ZnTe:N films.

Pressure	3 mTorr	6 mTorr	8 mTorr
N-doping w/o IS	2.39%	2.71%	3.15%
N-doping with IS	5.21%	6.08%	7.70%

Figure 5-15 shows the impacts of ion source on the structural properties of ZnTe:N films deposited at three different pressure levels. Figure 5-15 (a) shows the (111) peak positions of ZnTe:N films deposited with and without the ion source at various process pressures. The films deposited with or without the ion source showed ZnTe (111) peak in the θ-2θ XRD pattern. The (111) peak position was a function of process pressure and the use of the ion source. The peak position moved toward a higher 2θ for increasing process pressure. Also, for specific process pressure, the peak position moved toward higher 2θ for ion source enhanced deposition. This shift in the peak position is attributed to the higher level of N-doping in the film, in both cases.

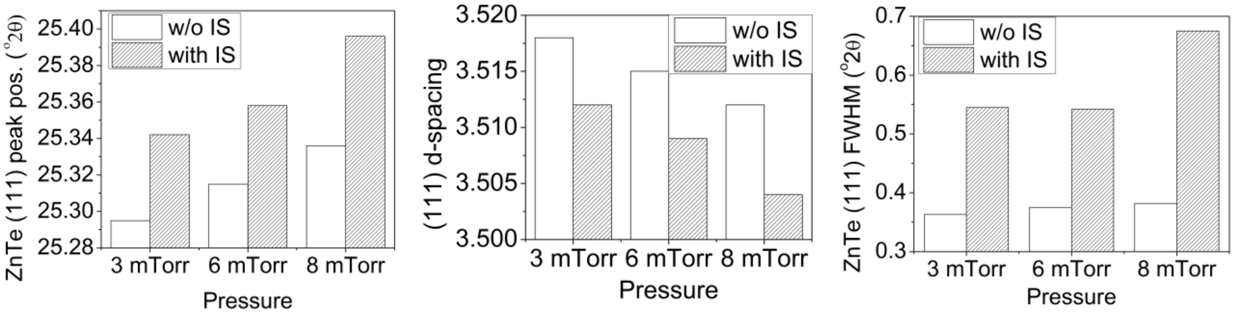

(a) (b) (c)

Figure 5-15. (a) (111) peak position, (b) (111) d-spacing, and (c) (111) FWHM of ZnTe:N films deposited with and without ion source at various process pressures.

Figure 5-15 (b) shows the d-spacing of the ZnTe (111) lattice of the films deposited with and without an ion source at various pressures. Ion source enhanced deposition could decrease the d-spacing for the (111) lattice, indicating the densification of the film by the ion source. Figure 5-15 (c) shows FWHMs of the (111) peak of the ZnTe:N films deposited with and without the ion source at various pressures. Without the ion source, the FWHMs were very similar for different pressure levels. However, ion source enhanced deposited films had broader FWHMs for all three process pressures. Ion source enhanced deposition caused more nucleation sites and smaller crystallites. This effect is assumed to produce a smoother surface with the densification of the film. Ion source enhanced deposited films, with smaller d spacing and wider FWHM, had a denser film with smaller crystallites.

5.5. Discussion and Conclusions

Nitrogen-doped ZnTe thin films were deposited with an only conventional magnetron and ion source assisted magnetron sputtering. Ion source enhanced magnetron sputtering was done using the magnetron with an additional ion source. The inclusion of the ion source could lower magnetron voltage, increase magnetron current and deposition rate, and enhance the quality of the deposited film. Ion source enhanced deposition could assist in improved nitrogen dopant uptake to the growing film, offering lower resistivity, higher transmittance, and denser microstructure of the film.

In conventional magnetron sputtering, nitrogen uptake and the conductivity of the film could also be increased by using a higher nitrogen flow of more than 5%. But the high nitrogen flow caused the transmittance of the film to go down. Ion source enhanced deposition could achieve high nitrogen uptake and low resistivity of ~30 Ohm-cm using nitrogen flow of only 2 – 5%, and with improved transmittance of the film. Magnetron power of 25 W with an ion source voltage of 120 V was found to be optimum for achieving low resistivity, lowest lattice d spacing, and highest FWHM. The film deposited with the ion source is assumed to have a denser film with smaller crystals than the film deposited without the ion source.

Ion source enhanced magnetron sputtering could result in higher nitrogen density in the ZnTe:N film than that of magnetron sputtering, at all pressure levels within studies. However, the ion source could lower the resistivity at 6 mTorr or lower pressures. The ion source decreased the d-spacing and increased the FWHM of the ZnTe cubic crystal structure at any process pressure. Ion source enhanced deposition could produce a denser film with smaller crystallites and decreased resistivity.

CHAPTER 6: FUTURE WORKS

This dissertation presents experimental findings on the growth of AlN thin films by pulsed DC and RF sputtering, in the presence of a mixture of plasma of argon and nitrogen gas. This work also presents experimental discoveries on ZnTe:N film growth by ion source enhanced magnetron sputtering in the presence of argon and nitrogen gas plasma. Following future research works can be carried out to understand the plasma characteristics, growth mechanism, and deposied film structure of reactive ion enhanced sputtering.

6.1. Nitrogen and Argon Plasma Discharge

The reactive ions and excited atoms present in the plasma affect the film growth and film properties significantly. Numerical simulations can be carried out to understand the N_2 + Ar discharge. The simulation results will give a detailed insight into the plasma properties, including ions density, ions distribution, ion flux on the substrate, and plasma potential between the target and the substrate. Experimental results can be obtained from the plasma discharge by measurements of the plasma parameters using a Langmuir probe and other suitable equipment. The effect of various process parameters such as pressure, target power, target power type, etc. on the plasma potential and plasma densities can also be studied.

6.2. Crystal-Embedded-in-Amorphous Structure

This dissertation proposes the crystal-embedded-in-amorphous structure for the ion source enhanced grown ZnTe:N film from the characterization data, such as XRD pattern and TEM images. Our experiments also found that the ZnTe:N film with the crystal-embedded-in-amorphous structure offered low resistivity than the nanocrystalline film with larger crystals. Simulations on carrier mobility and carrier transport mechanism can be carried out on the crystal-embedded-in-amorphous film to understand how this structure helps to lower the resistivity of the film. Further research studies can be carried out on the applicability of the crystal-embedded-in-amorphous structure in other films, such as transparent conductive oxide aiming solar cells and electronic display applications.

6.3. Nucleation and Initial Film Growth Under Ion Beam Bombardment

The nucleation and the initial growth influence the structural, electrical, mechanical, and surface-morphological properties of a thin film. The ion beam bombardment, during the ion source enhanced deposition, can impact the nucleation and initial film growth. In our research, we have demonstrated the effect of ion bombardment on the properties of the deposited film having a thickness of 100 nm. Numerical simulations and experimental research studies on the initial growth of the film can help to understand the reason behind the modulation of the structure and properties of the film deposited under the ion bombardment.

REFERENCES

REFERENCES

[1] J. Sarkar, Sputtering and Thin Film Deposition, Sputtering Materials for VLSI and Thin Film Devices. (2014) 93–170. https://doi.org/10.1016/B978-0-8155-1593-7.00002-3.

[2] Thin Film Processes, Hybrid Microcircuit Technology Handbook. (1998) 63–103. https://doi.org/10.1016/B978-081551423-7.50005-5.

[3] M. Aliofkhazraei, N. Ali, PVD Technology in Fabrication of Micro- and Nanostructured Coatings, Comprehensive Materials Processing. 7 (2014) 49–84. https://doi.org/10.1016/B978-0-08-096532-1.00705-6.

[4] B. Zheng, Y. Fu, K. Wang, T. Schuelke, Q.H. Fan, Electron dynamics in radio frequency magnetron sputtering argon discharges with a dielectric target, Plasma Sources Science and Technology. 30 (2021) 035019. https://doi.org/10.1088/1361-6595/ABE9F9.

[5] C. Fei, X. Liu, B. Zhu, D. Li, X. Yang, Y. Yang, Q. Zhou, AlN piezoelectric thin films for energy harvesting and acoustic devices, Nano Energy. 51 (2018) 146–161. https://doi.org/10.1016/J.NANOEN.2018.06.062.

[6] Q.H. Fan, T. Schuelke, L. Haubold, M. Petzold, Single beam plasma source, (2020).

[7] M. Ohring, Materials science of thin films, Elsevier, 2001.

[8] D. Schneider, T. Witke, T. Schwarz, B. Schoöneich, B. Schultrich, Testing ultra-thin films by laser-acoustics, Surface and Coatings Technology. 126 (2000) 136–141. https://doi.org/10.1016/S0257-8972(99)00672-6.

[9] P. Eaton, P. West, Atomic force microscopy, 2010.

[10] A.-A. Talukder, Plasma Treatment of Zinc Oxide Thin Film and Temperature Sensing Using the Zinc Oxide Thin Film, (2016). https://openprairie.sdstate.edu/etdhttps://openprairie.sdstate.edu/etd/1049 (accessed March 20, 2022).

[11] B. Fultz, J. Howe, Transmission electron microscopy and diffractometry of materials, 2012.

[12] B. Cullity, S. Stock, Elements of x-ray diffraction, 3rd ed., Prenrice hall, New Jersey, 2001.

[13] A. Iqbal, F. Mohd-Yasin, Reactive Sputtering of Aluminum Nitride (002) Thin Films for Piezoelectric Applications: A Review, Sensors. 18 (2018) 1797. https://doi.org/10.3390/s18061797.

[14] R. Turner, P. Fuierer, R. Newnham, T. Shrout, Materials for high temperature acoustic and vibration sensors: A review, Elsevier-Applied Acoustics. 41 (1994) 299–324. https://www.sciencedirect.com/science/article/pii/0003682X94900914 (accessed March 5, 2020).

[15] K. Mylvaganam, Y. Chen, W. Liu, M. Liu, L. Zhang, Hard thin films: Applications and challenges, Anti-Abrasive Nanocoatings. (2015) 543–567. https://doi.org/10.1016/B978-0-85709-211-3.00021-2.

[16] A.V. Singh, S. Chandra, G. Bose, Deposition and characterization of c-axis oriented aluminum nitride films by radio frequency magnetron sputtering without external substrate heating, Thin Solid Films. 519 (2011) 5846–5853. https://doi.org/10.1016/j.tsf.2011.02.074.

[17] D.L. Ma, H.Y. Liu, Q.Y. Deng, W.M. Yang, K. Silins, N. Huang, Y.X. Leng, Optimal target sputtering mode for aluminum nitride thin film deposition by high power pulsed magnetron sputtering, Vacuum. 160 (2019) 410–417. https://doi.org/10.1016/j.vacuum.2018.11.058.

[18] Y. Lu, M. Reusch, N. Kurz, A. Ding, T. Christoph, L. Kirste, V. Lebedev, A. Žukauskaitė, Surface Morphology and Microstructure of Pulsed DC Magnetron Sputtered Piezoelectric AlN and AlScN Thin Films, Physica Status Solidi (a). 215 (2018) 1700559. https://doi.org/10.1002/pssa.201700559.

[19] J. Kohout, J. Qian, T. Schmitt, R. Vernhes, O. Zabeida, J. Klemberg-Sapieha, L. Martinu, Hard AlN films prepared by low duty cycle magnetron sputtering and by other deposition techniques, Journal of Vacuum Science & Technology A: Vacuum, Surfaces, and Films. 35 (2017) 061505. https://doi.org/10.1116/1.4999460.

[20] S. Zhang, R. Xia, L. Lebrun, D. Anderson, T. Shrout, Piezoelectric materials for high power, high temperature applications, Materials Letters. 59 (2005) 3471–3475. https://www.sciencedirect.com/science/article/pii/S0167577X05005951 (accessed March 5, 2020).

[21] M. Akiyama, T. Kamohara, K. Kano, A. Teshigahara, Y. Takeuchi, N. Kawahara, Enhancement of piezoelectric response in scandium aluminum nitride alloy thin films prepared by dual reactive cosputtering, Advanced Materials. 21 (2009) 593–596. https://doi.org/10.1002/adma.200802611.

[22] Y. Saito, H. Takao, T. Tani, T. Nonoyama, K. Takatori, T. Homma, T. Nagaya, M. Nakamura, N.) Nbo, - Litao, - Lisbo, High Performance Lead-free Piezoelectric Material, R&D Review of Toyota CRDL. 41 (2006) 22–28. https://www.tytlabs.com/japanese/review/rev412pdf/412_022saito.pdf (accessed March 5, 2020).

[23] H. Fager, Growth and Characterization of Amorphous Multicomponent Nitride Thin Films, 2014. https://doi.org/10.3384/diss.diva-106576.

[24] A.C. Jones, S.A. Rushworth, D.J. Houlton, J.S. Roberts, V. Roberts, C.R. Whitehouse, G.W. Critchlow, Deposition of aluminum nitride thin films by MOCVD from the trimethylaluminum-ammonia adduct, Chemical Vapor Deposition. 2 (1996) 5–8. https://doi.org/10.1002/cvde.19960020102.

[25] R. Rodríguez-Clemente, B. Aspar, N. Azema, B. Armas, C. Combescure, J. Durand, A. Figueras, Morphological properties of chemical vapour deposited AlN films, Journal of Crystal Growth. 133 (1993) 59–70. https://doi.org/10.1016/0022-0248(93)90103-4.

[26] J.D. MacKenzie, C.R. Abernathy, S.J. Pearton, V. Krishnamoorthy, S. Bharatan, K.S. Jones, R.G. Wilson, Growth of AlN by metalorganic molecular beam epitaxy, Applied Physics Letters. 67 (1995) 253. https://doi.org/10.1063/1.114684.

[27] S. Six, J. Gerlach, B. Rauschenbach, Epitaxial aluminum nitride films on sapphire formed by pulsed laser deposition, Thin Solid Films. 370 (2000) 1–4. https://www.sciencedirect.com/science/article/pii/S0040609000009603 (accessed March 9, 2020).

[28] J. Sellers, Asymmetric bipolar pulsed DC: The enabling technology for reactive PVD, Surface and Coatings Technology. 98 (1998) 1245–1250. https://doi.org/10.1016/S0257-8972(97)00403-9.

[29] R.K. Choudhary, P. Mishra, A. Biswas, A.C. Bidaye, Structural and Optical Properties of Aluminum Nitride Thin Films Deposited by Pulsed DC Magnetron Sputtering, ISRN Materials Science. 2013 (2013) 759462. https://doi.org/10.1155/2013/759462.

[30] E. Blampain, O. Elmazria, O. Legrani, S.M. Murtry, Platinum/AlN/Sapphire SAW resonator operating in GHz range for high temperature Wireless SAW sensor, in: Joint UFFC, EFTF and PFM Symposium, IEEE, 2013: pp. 1081–1084. https://ieeexplore.ieee.org/abstract/document/6724817/ (accessed March 8, 2020).

[31] S. Yang, Y. Zhang, Y. Ai, Z. Cheng, L. Zhang, L. Jia, B. Dong, B. Zhang, J. Wang, J. Li, Impact of device parameters on performance of SAW resonators on AlN/Sapphire, Journal of Micromechanics and Microengineering PAPER. 28 (2018) 085005.

[32] C.-M. Lin, Y.-Y. Chen, V. Felmetsger, W.-C. Lien, V. v Felmetsger, T. Riekkinen, D.G. Senesky, A.P. Pisano, Surface acoustic wave devices on AlN/3C-SiC/Si multilayer structures, Journal of Micromechanics and Microengineering. 23 (2013) 8. https://doi.org/10.1088/0960-1317/23/2/025019.

[33] S. Fujii, High-frequency surface acoustic wave filter based on diamond thin film, Physica Status Solidi (A) Applications and Materials Science. 208 (2011) 1072–1077. https://doi.org/10.1002/pssa.201000064.

[34] M.T. Song, S.Y. Zhang, L. Fan, F.M. Zhou, Y. Wang, X.J. Shui, Study on sensitivities of Love-wave immunosensors based on SiO 2/36 YX-LiTaO3 and ZnO/36 YX-LiTaO3 structures, Acoustical Physics. 59 (2013) 528–532. https://doi.org/10.1134/S1063771013050217.

[35] L. Bo, C. Xiao, C. Hualin, M.A. Mohammad, T. Xiangguang, T. Luqi, Y. Yi, R. Tianling, Surface acoustic wave devices for sensor applications, Journal of Semiconductors. 37 (2016). https://doi.org/10.1088/1674-4926/37/2/021001.

[36] E. Dogheche, D. Remiens, S. Shikata, A. Hachigo, H. Nakahata, High-frequency surface acoustic wave devices based on LiNbO3 diamond multilayered structure, Applied Physics Letters. 87 (2005) 1–3. https://doi.org/10.1063/1.2135383.

[37] Y. Takagaki, T. Hesjedal, O. Brandt, K. Ploog, Surface-acoustic-wave transducers for the extremely-high-frequency range using AlN/SiC (0001), Semiconductor Science and Technology. 19 (2004) 256–259. https://iopscience.iop.org/article/10.1088/0268-1242/19/2/023 (accessed March 8, 2020).

[38] G. Bu, D. Čiplys, M. Shur, L.J. Schowalter, S. Schujman, R. Gaska, Surface acoustic wave velocity in single-crystal AlN substrates, IEEE Transactions on Ultrasonics, Ferroelectrics, and Frequency Control. 53 (2006) 251–254. https://doi.org/10.1109/TUFFC.2006.1588412.

[39] T. Aubert, O. Elmazria, M.B. Assouar, Wireless and batteryless surface acoustic wave sensors for high temperature environments, in: 9th International Conference on Electronic Measurement & Instruments, IEEE, Beijing, China, 2009: pp. 890–898. https://ieeexplore.ieee.org/abstract/document/5274413/ (accessed March 8, 2020).

[40] J. Prakash, G. Bose, Aluminum Nitride (AlN) Film Based Acoustic Devices: Material Synthesis and Device Fabrication, in: Marco G. Beghi (Ed.), Acoustic Waves - From Microdevices to Helioseismology, InTech, Milano, Italy, 2011: pp. 563–578. https://doi.org/10.5772/20840.

[41] M.A. Dubois, P. Muralt, Stress and piezoelectric properties of aluminum nitride thin films deposited onto metal electrodes by pulsed direct current reactive sputtering, Journal of Applied Physics. 89 (2001) 6389–6395. https://doi.org/10.1063/1.1359162.

[42] K.H. Chiu, J.H. Chen, H.R. Chen, R.S. Huang, Deposition and characterization of reactive magnetron sputtered aluminum nitride thin films for film bulk acoustic wave resonator, Thin Solid Films. 515 (2007) 4819–4825. https://doi.org/10.1016/j.tsf.2006.12.181.

[43] H. Cheng, Y. Sun, P. Hing, The influence of deposition conditions on structure and morphology of aluminum nitride films deposited by radio frequency reactive sputtering, Thin Solid Films. 434 (2003) 112–120. https://doi.org/10.1016/S0040-6090(03)00428-0.

[44] B.H. Hwang, C.S. Chen, H.Y. Lu, T.C. Hsu, Growth mechanism of reactively sputtered aluminum nitride thin films, Materials Science and Engineering A. 325 (2002) 380–388. https://doi.org/10.1016/S0921-5093(01)01477-0.

[45] J.P. Kar, G. Bose, S. Tuli, Correlation of electrical and morphological properties of sputtered aluminum nitride films with deposition temperature, Current Applied Physics. 6 (2006) 873–876. https://doi.org/10.1016/j.cap.2005.05.001.

[46] J.P. Kar, G. Bose, S. Tuli, Influence of nitrogen concentration on grain growth, structural and electrical properties of sputtered aluminum nitride films, Scripta Materialia. 54 (2006) 1755–1759. https://doi.org/10.1016/j.scriptamat.2006.01.038.

[47] M.B. Assouar, O. Elmazria, L. le Brizoual, P. Alnot, Reactive DC magnetron sputtering of aluminum nitride films for surface acoustic wave devices, Diamond and Related Materials. 11 (2002) 413–417. https://doi.org/10.1016/S0925-9635(01)00708-7.

[48] M.A. Dubois, P. Muralt, Stress and piezoelectric properties of aluminum nitride thin films deposited onto metal electrodes by pulsed direct current reactive sputtering, Journal of Applied Physics. 89 (2001) 6389–6395. https://doi.org/10.1063/1.1359162.

[49] Y. JuLee, S.-W. Kang, Growth of aluminum nitride thin films prepared by plasma-enhanced atomic layer deposition, Thin Solid Films. 446 (2004) 227–231. https://www.sciencedirect.com/science/article/pii/S0040609003013580 (accessed March 9, 2020).

[50] J.S. Cherng, D.S. Chang, Effects of pulse parameters on the pulsed-DC reactive sputtering of AlN thin films, Vacuum. 84 (2009) 653–656. https://doi.org/10.1016/J.VACUUM.2009.06.018.

[51] A. Ababneh, U. Schmid, J. Hernando, J.L. Sánchez-Rojas, H. Seidel, The influence of sputter deposition parameters on piezoelectric and mechanical properties of AlN thin films, Materials Science and Engineering B. 172 (2010) 253–258. https://www.sciencedirect.com/science/article/pii/S0921510710003983 (accessed March 31, 2020).

[52] E. Iborra, J. Olivares, M. Clement, L. Vergara, A. Sanz-Hervás, J. Sangrador, Piezoelectric properties and residual stress of sputtered AlN thin films for MEMS applications, Sensors and Actuators, A: Physical. 115 (2004) 501–507. https://doi.org/10.1016/j.sna.2004.03.053.

[53] B. Fritsche, T. Chevolleau, J. Kourtev, A. Kolitsch, W. Möller, Plasma diagnostic of an RF magnetron Ar/N2discharge, in: Vacuum, Elsevier Ltd, 2002: pp. 139–145. https://doi.org/10.1016/S0042-207X(02)00322-6.

[54] N. Dyatko, Y. Ionikh, A. Napartovich, Influence of Nitrogen Admixture on Plasma Characteristics in a dc Argon Glow Discharge and in Afterglow, Atoms. 7 (2019) 13. https://doi.org/10.3390/atoms7010013.

[55] L. Shu, B. Peng, C. Li, D. Gong, Z. Yang, X. Liu, W. Zhang, The Characterization of Surface Acoustic Wave Devices Based on AlN-Metal Structures, Sensors. 16 (2016) 526. https://doi.org/10.3390/s16040526.

[56] R. Mock, H. Meixner, A miniaturized high-temperature pressure sensor for the combustion chamber of a spark ignition engine, Elsevier-Sensors and Actuators: A. Physical. 25 (1991) 103–106.

https://www.sciencedirect.com/science/article/pii/092442479087015B (accessed March 5, 2020).

[57] H. Bartsch, R. Grieseler, J. Mánuel, J. Pezoldt, J. Müller, Magnetron Sputtered AlN Layers on LTCC Multilayer and Silicon Substrates, Coatings. 8 (2018) 289. https://doi.org/10.3390/coatings8080289.

[58] A.V. Singh, S. Chandra, A.K. Srivastava, B.R. Chakroborty, G. Sehgal, M.K. Dalai, G. Bose, Structural and optical properties of RF magnetron sputtered aluminum nitride films without external substrate heating, Applied Surface Science. 257 (2011) 9568–9573. https://doi.org/10.1016/j.apsusc.2011.06.065.

[59] M.H. Park, S.H. Kim, Thermal conductivity of AlN thin films deposited by RF magnetron sputtering, Materials Science in Semiconductor Processing. 15 (2012) 6–10. https://doi.org/10.1016/j.mssp.2011.04.007.

[60] H. Bartsch, R. Grieseler, J. Mánuel, J. Pezoldt, J. Müller, Magnetron sputtered AlN layers on LTCC multilayer and silicon substrates, Coatings. 8 (2018). https://doi.org/10.3390/coatings8080289.

[61] M.H. Park, S.H. Kim, Thermal conductivity of AlN thin films deposited by RF magnetron sputtering, Materials Science in Semiconductor Processing. 15 (2012) 6–10. https://doi.org/10.1016/j.mssp.2011.04.007.

[62] F. Liu, J. Zhu, Y. Xu, L. Zhou, Y. Li, L. Hu, J. Yao, S. Dai, SnX (X = S, Se) thin films as cost-effective and highly efficient counter electrodes for dye-sensitized solar cells, Chemical Communications. 51 (2015) 8108–8111. https://doi.org/10.1039/C5CC00772K.

[63] D.H. Cho, W.J. Lee, S.W. Park, J.H. Wi, W.S. Han, J. Kim, M.H. Cho, D. Kim, Y.D. Chung, Non-toxically enhanced sulfur reaction for formation of chalcogenide thin films using a thermal cracker, Journal of Materials Chemistry A. 2 (2014) 14593–14599. https://doi.org/10.1039/C4TA02507E.

[64] H. Singh, M. Singh, J. Singh, B.S. Bansod, T. Singh, A. Thakur, M.F. Wani, J. Sharma, Composition dependence study of thermally evaporated nanocrystalline ZnTe thin films, Journal of Materials Science: Materials in Electronics. 30 (2019) 3504–3510. https://doi.org/10.1007/s10854-018-00627-9.

[65] T.M. Shimpi, J. Drayton, D.E. Swanson, W.S. Sampath, Properties of Nitrogen-Doped Zinc Telluride Films for Back Contact to Cadmium Telluride Photovoltaics, Journal of Electronic Materials 2017 46:8. 46 (2017) 5112–5120. https://doi.org/10.1007/S11664-017-5502-0.

[66] A.E. Rakhshani, S. Thomas, Nitrogen doping of ZnTe for the preparation of ZnTe/ZnO light-emitting diode, Journal of Materials Science. 48 (2013) 6386–6392. https://doi.org/10.1007/s10853-013-7438-y.

[67] B. Späth, J. Fritsche, A. Klein, W. Jaegermann, Nitrogen doping of ZnTe and its influence on CdTe⁄ZnTe interfaces, Applied Physics Letters. 90 (2007) 062112. https://doi.org/10.1063/1.2459589.

[68] A.E. Rakhshani, S. Thomas, Nitrogen doping of ZnTe for the preparation of ZnTe/ZnO light-emitting diode, Journal of Materials Science. 48 (2013) 6386–6392. https://doi.org/10.1007/S10853-013-7438-Y/FIGURES/7.

[69] E. Chason, S.T. Picraux, J.M. Poate, J.O. Borland, M.I. Current, T. Diaz De La Rubia, D.J. Eaglesham, O.W. Holland, M.E. Law, C.W. Magee, J.W. Mayer, J. Melngailis, A.F. Tasch, Ion beams in silicon processing and characterization, Journal of Applied Physics. 81 (1998) 6513. https://doi.org/10.1063/1.365193.

[70] H. Ji, G.S. Was, J.W. Jones, N.R. Moody, Effect of ion bombardment on in-plane texture, surface morphology, and microstructure of vapor deposited Nb thin films, Journal of Applied Physics. 81 (1998) 6754. https://doi.org/10.1063/1.365217.

[71] M.W. Thompson, II. The energy spectrum of ejected atoms during the high energy sputtering of gold, Https://Doi.Org/10.1080/14786436808227358. 18 (2010) 377–414. https://doi.org/10.1080/14786436808227358.

[72] T.M. Shimpi, J. Drayton, D.E. Swanson, W.S. Sampath, Properties of Nitrogen-Doped Zinc Telluride Films for Back Contact to Cadmium Telluride Photovoltaics, Journal of Electronic Materials. 46 (2017) 5112–5120. https://doi.org/10.1007/S11664-017-5502-0.

[73] C.S. Ferekides, D. Marinskiy, V. Viswanathan, B. Tetali, V. Palekis, P. Selvaraj, D.L. Morel, High efficiency CSS CdTe solar cells, Thin Solid Films. C (2000) 520–526. https://doi.org/10.1016/S0040-6090(99)00824-X.

[74] J. Britt, C. Ferekides, Thin-film CdS/CdTe solar cell with 15.8% efficiency, Applied Physics Letters. 62 (1998) 2851. https://doi.org/10.1063/1.109629.

[75] D.L. Bätzner, A. Romeo, M. Terheggen, M. Döbeli, H. Zogg, A.N. Tiwari, Stability aspects in CdTe/CdS solar cells, Thin Solid Films. 451–452 (2004) 536–543. https://doi.org/10.1016/J.TSF.2003.10.141.

[76] K.D. Dobson, I. Visoly-Fisher, G. Hodes, D. Cahen, Stability of CdTe/CdS thin-film solar cells, Solar Energy Materials and Solar Cells. 62 (2000) 295–325. https://doi.org/10.1016/S0927-0248(00)00014-3.

[77] I.W. Tao, M. Jurkovic, W.I. Wang, Doping of ZnTe by molecular beam epitaxy, Applied Physics Letters. 64 (1998) 1848. https://doi.org/10.1063/1.111775.

[78] H. Singh, T. Singh, A. Thakur, J. Sharma, Structural analysis of nanocrystalline ZnTe alloys synthesized by melt quenching technique, AIP Conference Proceedings. 1953 (2018) 030073. https://doi.org/10.1063/1.5032408.

[79] J. Han, T.S. Stavrinides, M. Kobayashi, R.L. Gunshor, M.M. Hagerott, A. v. Nurmikko, Heavy p-doping of ZnTe by molecular beam epitaxy using a nitrogen plasma source, Applied Physics Letters. 62 (1998) 840. https://doi.org/10.1063/1.108568.

[80] K.S. Lee, G. Oh, E.K. Kim, Growth of p-type ZnTe thin films by using nitrogen doping during pulsed laser deposition, Journal of the Korean Physical Society. 67 (2015) 672–675. https://doi.org/10.3938/jkps.67.672.

[81] M.S. Bhagwat, Z. Han, S.K. Ng, U. Palt, S. Sahat, A.K. Chaudhurit, V. v Raot, H.D. Banerjees, Some optical properties of evaporated zinc telluride films, Journal of Physics D: Applied Physics. 22 (1989) 965. https://doi.org/10.1088/0022-3727/22/7/014.